UNIVERSITY OF COPENHAGEN

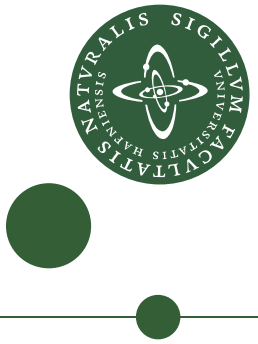

Master Thesis

Morten Canth Hels

Toward entanglement detection

Non-collinear spin-orbit magnetic fields in a bent carbon nanotube

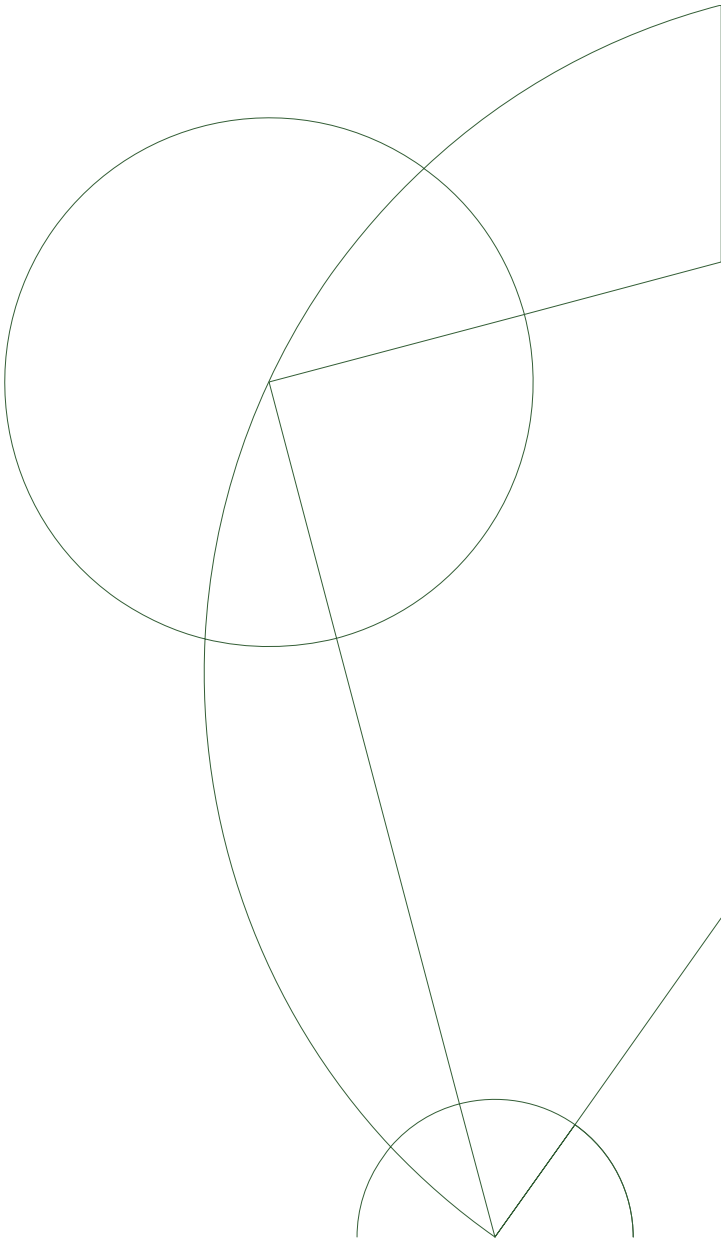

Supervisors: Jesper Nygård & Kasper Grove-Rasmussen

Submitted on October 9, 2015

Dansk resume

Opsplitningen af sammenfiltrede kvantetilstande er en betingelse for mange algoritmer inden for kvanteinformation. En superleder er en naturlig kilde til Cooper par som er sammenfiltrede par af elektroner. Dette speciale beskriver fabrikation og lav-temperatur-målinger af et kulstofnanorør Cooper par splitter-apparat som består af to parallelle kvanteprikker med en fælles superledende kontakt.

Bias spektroskopi-målinger viser, at apparatet er af høj kvalitet sådan at individuelle kvantetilstandes karakter kan identificeres i prikkerne. Excitationsspektroskopi-data viser, at spin-bane koblingen delvist dominerer spektret og at spin-bane magnetfelterne på to forskellige sider af en krumning i nanorøret er ikke-collineære. Ved at gøre den superledende film tynd øges det kritiske magnetfelt i planen med omkring 70 gange dets normale værdi. Stærk kobling mellem prikkerne og kontakterne reducerer muligheden for at anvende dette specifikke apparat til at opsplitte Cooper par.

Resultaterne som præsenteres i dette speciale tegner lovende for at udføre en måling af sammenfiltringen i Cooper par som beskrevet i et nyligt teoretisk forslag.

Abstract

Splitting entangled quantum states is a requirement for many quantum information algorithms. A superconductor is a natural source of Cooper pairs which are entangled pairs of electrons. This master thesis describes the fabrication and low-temperature measurement of a carbon nanotube Cooper pair splitter device which consists of two parallel quantum dots with a common superconducting lead.

Bias spectroscopy measurements show that the device is of high quality such that the character of individual quantum states can be identified in the dots. Excitation spectroscopy data reveal that spin-orbit interaction partially dominates the spectrum and that the spin-orbit magnetic fields on opposite sides of a bend in the nanotube are non-collinear. By making the superconducting film thin the critical in-plane magnetic field is increased to about 70 times its bulk value. Strong coupling between the dots and the leads reduces the use of this specific device as a Cooper pair splitter.

The results presented in this thesis shows promise for conducting an entanglement detection measurement following a recent theoretical proposal.

Contents

List of Figures

List of Tables

Chapter 1

Introduction

As Moore's law is starting to fail due to fundamental constraints candidates are being considered as replacements for traditional silicon computing. Quantum computing is one of these candidates.

Classical computers come up short when dealing with problems of a certain size or complexity like simulating superconductors or protein folding. A quantum computer replaces the classical bit with a qubit (quantum bit). By doing so it enables the use of new and faster algorithms that are capable of dealing with larger and more complex problems than are classical computers.

A key element for these algorithms is the entangled state and being able to reliably generate entangled states is key to building a quantum computer. Given two qubits and two states $|0\rangle$ and $|1\rangle$ an entangled state is one which can not be written as a product of two single-qubit states. For instance,

$$|\psi\rangle = |0\rangle\,|0\rangle + |1\rangle\,|1\rangle \tag{1.1}$$

is an entangled state because products of single-particle states $|\phi\rangle = |0\rangle + |1\rangle$ inevitably includes cross-terms like $|0\rangle\,|1\rangle$.

A natural source of entangled pairs is the superconducting condensate. Cooling a metal to cryogenic temperatures causes its conduction electrons to rearrange into so-called Cooper pairs which have opposite momentum and spin. The wave function of a Cooper pair can be expressed as

$$|\psi\rangle_{\,\mathrm{BCS}} = u\,|0\rangle\,|0\rangle + v\,|\mathbf{k}\uparrow\rangle\,|-\mathbf{k}\downarrow\rangle\,, \tag{1.2}$$

that is, the states $|\mathbf{k}\uparrow\rangle$ and $|-\mathbf{k}\downarrow\rangle$ must be simultaneously occupied. A Cooper pair is an entangled state which is hinted at by the similarity of its wave function above with (1.1). If the Cooper pair can be split into its constituent electrons we have, in principle, our entangled state.

In a quantum dot electrons are made to tunnel one-by-one through a constricted region by utilizing their mutual repulsion. A Cooper pair

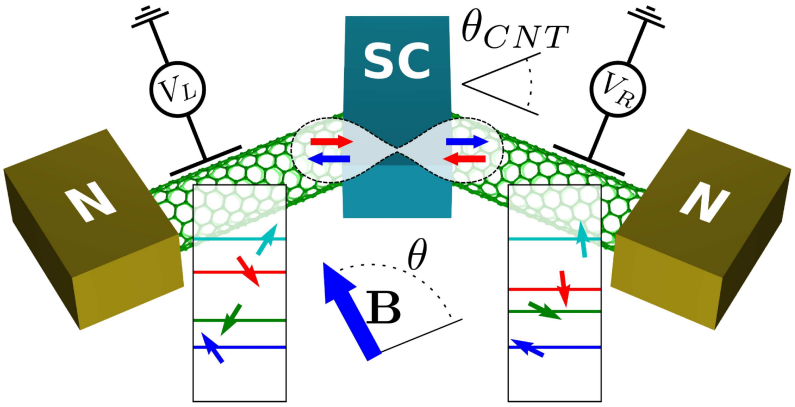

Figure 1.1: A schematic of the Braunecker proposal (Braunecker *et al.* [1]). Cooper pairs are ejected from a central superconductor (SC) and cause a nonlocal current in the two nanotube quantum dots. The current depends on the overlap between the spin of the Cooper pair electrons (horizontal arrows) and the spin of the nanotube states (slanted arrows). Measuring the current for all 16 combinations of the states in the nanotube segments reveals whether the particles responsible for the current are entangled. In order to obtain dissimilar splittings of the levels in the two nanotube segments the nanotubes must be at an angle.

is not allowed in quantum dots because of this repulsion. Thus, if the Cooper pair electrons were to leave the superconductor through a quantum dot they would have to separate and tunnel through different dots. Figure 1.1 shows this situation where carbon nanotubes play the role as quantum dots.

Experiments of this type have already been done by measuring a correlation in current between the two quantum dots. Also, Cooper pair splitting (CPS) in both carbon nanotubes [2, 3] and nanowires [4–6] has been demonstrated. What remains to be seen is that the electrons are actually entangled when they leave the superconductor.

This question is addressed in the proposal by Braunecker *et al.* [1] shown schematically in Figure 1.1. The idea is to use kinked carbon nanotubes with spin-orbit coupling as spin-filters so that the current is suppressed for certain filter configurations. For instance, splitting a Cooper pair through two spin-up states in the nanotubes should yield a lower current than splitting it through states with opposite spin. This type of correlation test is called a Bell test. Carbon nanotubes are especially well suited for this purpose since the coupling between spin and orbital motion gives rise to a built-in magnetic field oriented parallel to the tube axis. When an external magnetic field is applied we can calculate the spin direction of the states in the nanotube and orient the "filter" as we choose, thus enabling us to do controlled correlation measurements. It is essential the the nanotubes are at an angle so that their built-in magnetic fields are non-collinear.

We can sum up the requirements for the Braunecker proposal as follows:

1. The states in the carbon nanotube should be identifiable, that is, the quantum dot should exhibit four-fold periodicity.

2. A superconducting gap must be present in a bias spectroscopy plot to indicate that the central lead is superconducting.

3. The critical magnetic field B_C of the superconductor must not be much lower than the spin-orbit magnetic field. Otherwise the superconductor will be made normal before the field can appreciably alter the nanotube spectrum at a value of about $B \sim B_{SO}$.

4. In order to have reasonably well-defined spin states we require that spin-orbit interaction dominates disorder: $\Delta_{SO} > \Delta_{KK'}$.

5. The spin-orbit magnetic fields must not be parallel to ensure that the spin bases are not parallel. Consequently, the nanotube segments themselves must be at an angle.

6. Finally, the current should exhibit non-local correlations in a specific pattern.

Several of the requirements above have already been demonstrated previously in separate devices. Carbon nanotubes quantum dots exhibiting four-fold symmetry and with superconducting gaps are common and can be seen in, e.g., [7]. Getting a high critical magnetic field is a matter of choosing the right material or making the superconducting film thin. Spin-orbit dominated nanotubes have been mostly demonstrated in so-called "clean" devices [8], but also in a regular non-clean device [9]. Some bent (or kinked) nanotubes have been measured previously, e.g., [10]. Cooper pair splitting has been shown only recently but the mechanisms behind the splitting are not well understood.

Outline of this thesis

This 60 ECTS points thesis is written as part of an integrated (4+4) PhD program. The problem statement of the work leading to this thesis is the following:

Fabricate and measure a carbon nanotube Cooper pair splitter (CNT-CPS) device which satisfies the requirements for the Braunecker proposal.

In Chapter 2 relevant theory about carbon nanotubes and quantum dots will be reviewed. Chapter 3 concerns describes fabrication considerations and measurement setup for a specific CNT-CPS device. Note that detailed fabrication recipes are available in the appendix. Chapter 4 presents data and analysis of the device described in Chapter 3.

Chapter 2

Theory

2.1 Carbon Nanotubes

In this section we present an overview of the electronic structure of carbon nanotubes. Focus will be on the effects that will be discussed in the data which means that, e.g., strain and torsion effects will not be considered. A more complete treatment can be found in [11] which also serves as inspiration for the present section.

2.1.1 Physical Structure

A carbon nanotube (CNT) is a cylinder made of carbon atoms bonded in a hexagonal structure.

For analyzing both physical and electronic properties the nanotube can be thought of as a rolled-up graphene sheet as shown in Figure 2.1. The graphene unit cell consists of two inequivalent carbon atoms, A and B. The translation vectors are $\mathbf{a}_1$ and $\mathbf{a}_2$. We can form a cylinder from the sheet by defining the chiral vector

$$\mathbf{C}_h = n\mathbf{a}_1 + m\mathbf{a}_2 \tag{2.1}$$

and rolling the sheet along it until the start and end points of the chiral vector touch. Examples of the resulting cylinder are shown in Figure 2.2. In the general case the tube will be chiral so that its mirror image represents a different structure which can not be obtained from rotation. Using the short-hand notation $\mathbf{C}_h = (n, m)$ we see that two cases have a special symmetry: $(n, 0)$ (zig-zag) and (n, n) (arm-chair). These tubes are non-chiral, i.e., mirroring yields an equivalent structure.

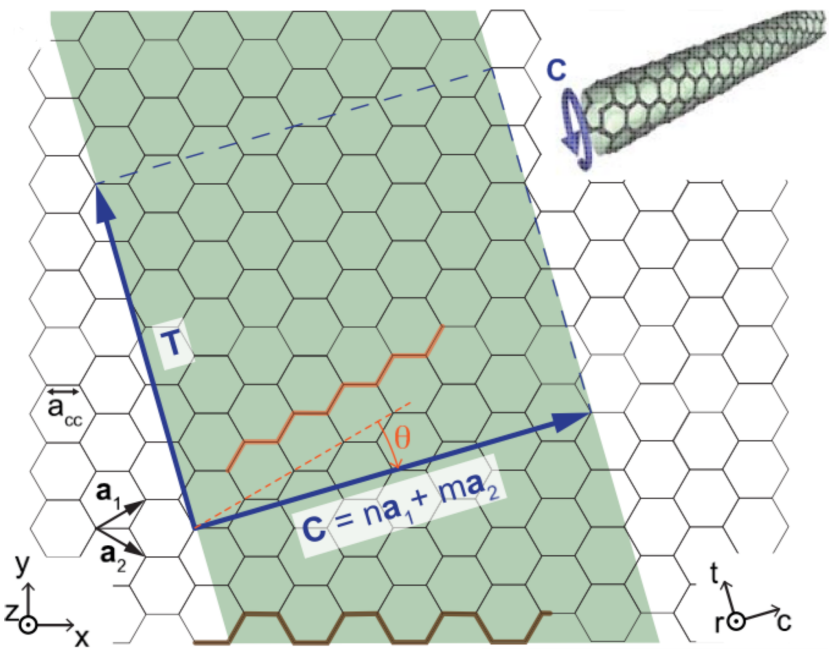

Figure 2.1: A nanotube is obtained from a sheet of graphene by "rolling" the sheet along **C**. The area defined by the **T** and **C** vectors define the surface of the nanotube. The chiral vector **C** determines various properties of the nanotube through the angle θ. Since a nanotube exhibits cylindrical symmetry the graphene coordinates x, y, z are transformed into t, r, c coordinates for the nanotube, denoting the axial, radial and circumferential direction, respectively. Figure adapted from Laird *et al.* [11].

The angle θ between a_1 and the chiral vector $\mathbf{C}_h$ is important for the properties of the CNT. It is given by

$$\cos\theta = \frac{\mathbf{C}_h \cdot \mathbf{a}_1}{|\mathbf{C}_h||\mathbf{a}_1|} = \frac{2a+b}{2\sqrt{a^2+ab+b^2}} \tag{2.2}$$

For the zig-zag and armchair structures $\theta = 0°$ and $30°$, respectively.

In graphene the distance between nearest neighbors $a_{\mathrm{CC}} = 0.142\,\mathrm{nm}$. The diameter D of the CNT can be calculated with

$$D = \frac{\sqrt{3}a_{\mathrm{CC}}}{\pi}\sqrt{a^2+ab+b^2} \tag{2.3}$$

which also equals $|\mathbf{C}_h|/\pi$. Typical nanotube diameters are 1-6 nm.

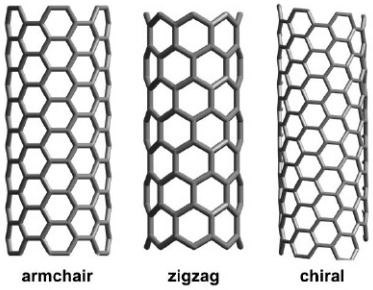

Figure 2.2: The chiral vector $\mathbf{C}_h$ defines the chirality of the CNT as either armchair, zigzag or chiral. Armchair: $\mathbf{C}_h = (n, n)$, zigzag: $\mathbf{C}_h = (n, 0)$. All other vectors give chiral nanotubes. Adapted from [12].

2.1.2 Electronic Structure

The starting point for the CNT band structure is the graphene spectrum which we'll review first, before going into the corrections necessary for nanotubes. The important part of the graphene spectrum are the Dirac cones which are located at the Dirac points $\mathbf{K}, \mathbf{K}' = (0, \mp)4\pi/3a_{\mathrm{CC}}$. The Dirac points $\mathbf{K}$ and $\mathbf{K}'$ are a time-reversed pair, so by Kramers theorem they must have the same energy as long as time-reversal symmetry is not broken. Near the Dirac points the dispersion is approximately linear so with E_{F} as the zero-point of energy and measuring $\boldsymbol{\kappa}$ from a Dirac point we can write

$$E = \pm\hbar v_{\mathrm{F}}|\boldsymbol{\kappa}|. \tag{2.4}$$

Here v_F is the Fermi velocity of graphite which is about 8×10^5 m/s.

For the purposes of this thesis we consider the following perturbations to the graphene spectrum:

1. Quantization of the circumferential k-component $k_\perp$ which confines the spectrum to lines in the graphene spectrum.
2. Curvature-induced shift of the Dirac cones.
3. Application of an external magnetic field.
4. Spin-orbit coupling between the spin of an electron and its motion around the nanotube.
5. A disorder term $\Delta_{KK'}$ which mixes the circumferential modes K and K'.

Quantization of $k_\perp$ Rolling up a graphene sheet puts restrictions on $k_\perp$ which is unrestricted in graphene. For the wave function to be single-valued we require that it does not change its value upon completing one revolution around the nanotube:

$$\exp(i\mathbf{kr}) = \exp(i\mathbf{k}(\mathbf{r}+\mathbf{C})) \Rightarrow \mathbf{k}\cdot\mathbf{C} = 2\pi p \Rightarrow k_\perp = 2p/D \qquad (2.5)$$

where p is an integer. Restricting $k_\perp$ in this way yields a spectrum consisting of line cuts through the graphene spectrum as shown in Figure 2.3.

Depending on whether the cuts miss the Dirac points or pass through them the low-energy dispersion will be either linear or hyperbolic. In the latter case a gap opens up since the conduction and valence bands don't touch at $|\kappa_\parallel| = 0$. When $k_\perp$ is quantized the dispersion takes the form

$$E = \pm\sqrt{\hbar^2 v_F^2 \kappa_\parallel^2 + E_G^2/4} \qquad (2.6)$$

Metallic nanotubes have linear dispersions and are gapless while semiconducting nanotubes have hyperbolic dispersions and show gaps of

$$E_G = 4\hbar v_F/3D \approx 700\,\text{meV}/D[\text{nm}]. \qquad (2.7)$$

Anticipating its use for quantum dots we replace $\hbar v_F \kappa_\parallel$ in (2.6) by the confinement energy E_{conf}:

$$E = \pm\sqrt{E_{conf}^2 + E_G^2/4} \qquad (2.8)$$

In quantum dots the longitudinal motion is confined which leads to quantized values for $\kappa_\parallel$ and hence E_{conf}. States that have the same E_{conf} are said to belong to the same shell.

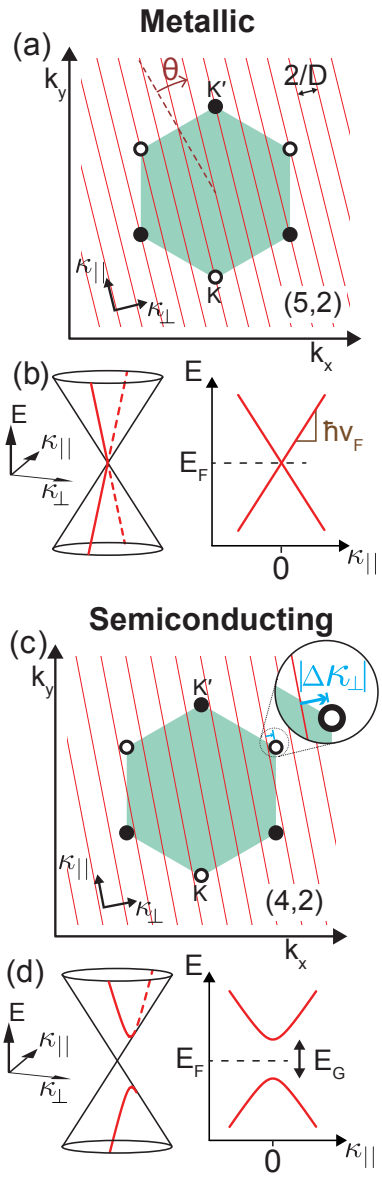

Figure 2.3: **(a), (c)** By quantizing the wave number $k_\perp$ around the nanotube circumference the 1D dispersion of a nanotube is obtained as shown in **(b), (d)**. If the red quantization lines pass through a Dirac point (circles) the nanotube is nominally metallic, while a band gap E_G opens in the opposite case. Figure adapted from Laird *et al.* [11].

In Figure 2.3 we see that a quantization line that passes close to a $\mathbf{K}$ point will also pass close to a $\mathbf{K}'$ point in the same distance. The states on these lines close to the $\mathbf{K}$ and $\mathbf{K}'$ points constitute the low-energy dispersion. It is convenient to classify them as K or K' states according to which type of point they are close to. This enables us to make the intuitive interpretation that K and K' states in the same band (conduction or valence) circulate the nanotube in opposite directions because they are time-reversal conjugates. The direction of circulation is opposite for states in the conduction and valence bands since $v_\perp \propto \partial E/\partial k_\perp$ has opposite signs in the conduction and valence bands.

The K and K' points are collectively known as the *valley* quantum number. We'll use $\tau = \pm 1$ to refer to the valley quantum number where $\tau = +1$ (-1) corresponds to K (K').

The K states are time-reversed partners of the K' states so they are degenerate when time-reversal symmetry is not broken. This makes the total degeneracy in nanotubes equal to four since the states are also spin-degenerate.

Curvature-induced displacement of Dirac cones Another consequence of rolling up a graphene sheet is that the orbital overlaps of the carbon atoms change. This displaces the Dirac cones by a vector $\mathbf{\Delta}\kappa^{\mathrm{cv}}$ which is opposite for K and K'. In some metallic nanotubes this displacement causes the quantization line to no longer go through the Dirac points. These nanotubes are thus no longer gapless but exhibit gaps of [11]

$$E_{\mathrm{G}}^{\mathrm{cv}} = 2\hbar v_{\mathrm{F}} |\Delta\kappa_\perp^{\mathrm{cv}}| \tag{2.9}$$

where the cv superscript stands for curvature. Nanotubes that change character in this way are called narrow-gap nanotubes. The magnitude of the curvature band gap is about

$$E_{\mathrm{G}}^{\mathrm{cv}} \sim \frac{50\,\mathrm{meV}}{D[\mathrm{nm}]^2} \cos 3\theta \tag{2.10}$$

which is always smaller than the quantization band gap in (2.7) so that semiconducting nanotubes remain semiconducting. Armchair nanotubes remain metallic with the curvature perturbation since in their case $\mathbf{\Delta}\kappa^{\mathrm{cv}}$ is parallel to the quantization lines and $k_\perp^{\mathrm{cv}} = 0$.

Behavior in Magnetic Fields A magnetic field interacts with an electron orbiting a CNT in two ways: By coupling to the electron spin (Zeeman effect) and by coupling to the circumferential motion around the nanotube.

The Zeeman energy in a magnetic field oriented parallel to the nan-

otube axis is

$$E_{\mathrm{Z}} = \frac{1}{2} g_{\mathrm{s}} \mu_{\mathrm{B}} s B_{\parallel} \tag{2.11}$$

where $s = \pm 1$ denotes spin parallel or anti-parallel to the nanotube axis.

To find the energy of the coupling between the circumferential motion and the magnetic field we use the following classical argument: The nanotube cross-section has an area $A = \pi D^2/4$ and the electron carries a current $I = |e| v_{\mathrm{F}}/\pi D$ by orbiting the tube. This gives for the magnitude of the orbital magnetic moment

$$\mu_{\mathrm{orb}} = IA = |e| \frac{v_{\mathrm{F}}}{\pi D} \cdot \pi D^2/4 = |e| v_{\mathrm{F}} D/4. \tag{2.12}$$

To obtain the orbital magnetic moment for a specific state we multiply by τ which determines the direction of circulation. Applying a magnetic field parallel $B_{\parallel}$ as in Figure 2.4 thus increases the energy of the electron by

$$E_{\mathrm{orb}} = \mp \tau \mu_{\mathrm{orb}} B_{\parallel}. \tag{2.13}$$

where the minus (plus) is for the conduction (valence) band. This equation fixes our convention regarding valley interaction with a magnetic field: K states ($\tau = +1$) in the conduction band *decrease* in energy with *increasing* parallel magnetic field. By defining an orbital g-factor[1]

$$g_{\mathrm{orb}} = \mu_{\mathrm{orb}}/\mu_{\mathrm{B}} = \frac{1}{4} D e v_{\mathrm{F}} \approx 3.5 \times D[\mathrm{nm}] \tag{2.14}$$

we can write

$$E_{\mathrm{orb}} = \mp \tau g_{\mathrm{orb}} \mu_{\mathrm{B}} B_{\parallel} \tag{2.15}$$

so that the total energy E_{mag} due to a parallel magnetic field is given by

$$E_{\mathrm{mag}} = E_{\mathrm{Z}} + E_{\mathrm{orb}} = (s g_{\mathrm{s}} \mp \tau g_{\mathrm{orb}}) \mu_{\mathrm{B}} B_{\parallel}. \tag{2.16}$$

A rigorous derivation of the orbital interaction involves the Aharonov-Bohm flux through the nanotube cross section. The result obtained in this way is the same as the one above, though.

In a magnetic field with arbitrary orientation the spin-up and spin-down states are mixed by the perpendicular field, but only within a valley.

The nanotube spectrum as a function of perpendicular and parallel magnetic field is shown in Figure 2.5. In a parallel field $s g_{\mathrm{s}}$ and τg_{orb} add to give four slopes. Two doubly-degenerate lines are visible for a perpendicular field because it does not break the valley degeneracy.

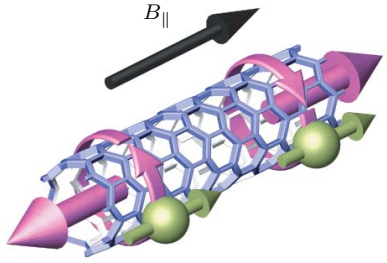

Figure 2.4: Schematic showing orbital angular momentum (purple), spin angular momentum (green) and applied $B_{\parallel}$-field. Adapted from [8].

[1] Sometimes g_{orb} is defined as $g_{\mathrm{orb}} = 2\mu_{\mathrm{orb}}/\mu_{\mathrm{B}}$ so that we get the same factor of 1/2 as in (2.11) in the expression for E_{orb}.

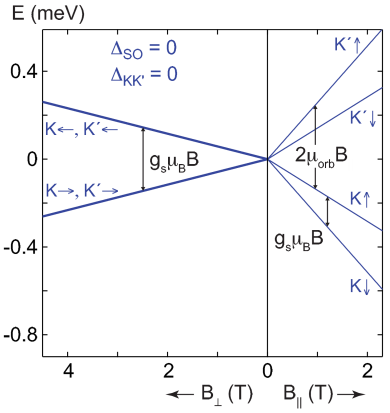

Figure 2.5: Nanotube spectrum without spin-orbit coupling or disorder effects. In a parallel magnetic field the states split up according to their combined g-factor $s g_{\mathrm{s}} \mp \tau g_{\mathrm{orb}}$. A perpendicular field only affects the spin because the orbital motion is perpendicular to the field. Figure adapted from Laird *et al.* [11].

Spin-orbit Coupling The interaction between the spin of an electron and the orbit in which it moves is called spin-orbit coupling. For instance, an electron moving with velocity $\mathbf{v}$ in the electric field $\mathbf{E}$ of an atomic nucleus will experience a magnetic field

$$\mathbf{B} = -\frac{1}{c^2}(\mathbf{v} \times \mathbf{E}). \tag{2.17}$$

This magnetic field then couples with the electron spin. For this electron the "orbit" in spin-orbit coupling is an actual orbit around the atomic nucleus.

In carbon nanotubes the "orbit" is the motion around the circumference of the tube. In cylindrical coordinates this motion is in the azimuthal direction while the average electric field from the nanotube atoms is in the radial direction for symmetry reasons. Thus, an electron orbiting a nanotube experiences a magnetic field which is directed parallel to the nanotube axis. This property is important for the Braunecker proposal.

A closer theoretical treatment reveals that there are two types of spin-orbit coupling in carbon nanotubes: A Zeeman-like contribution which shifts the Dirac cones up or down by an amount

$$\Delta E^{\mathrm{SO,Z}}(\tau, s) = \Delta^0_{\mathrm{SO}} \tau s, \tag{2.18}$$

and an orbital-like contribution which shifts the Dirac cones horizontally by an amount

$$\Delta\kappa_\perp^{\mathrm{SO,orb}}(s) = -s\frac{\Delta^1_{\mathrm{SO}}}{\hbar v_{\mathrm{F}}}. \tag{2.19}$$

The Zeeman-like term is simply added to the Hamiltonian while the orbital-like contribution is added to the curvature shift of the Dirac cones.

At zero magnetic field with only spin-orbit coupling present the splitting of the four states is given by

$$\Delta_{\mathrm{SO}} \equiv 2\left(\Delta^0_{\mathrm{SO}} \mp \Delta^1_{\mathrm{SO}}\frac{g_{\mathrm{orb}}}{g^0_{\mathrm{orb}}}\right). \tag{2.20}$$

The data presented in this thesis does not allow distinguishing the two types of spin-orbit coupling so we will be using only the Δ_{SO} parameter. We can also define a spin-orbit magnetic field $\mathbf{B}_{\mathrm{SO}}$ by taking Δ_{SO} as the Zeeman splitting of this field:

$$\Delta_{\mathrm{SO}} = g_{\mathrm{s}}\mu_{\mathrm{B}}B_{\mathrm{SO}} \Rightarrow B_{\mathrm{SO}} = \frac{\Delta_{\mathrm{SO}}}{g_{\mathrm{s}}\mu_{\mathrm{B}}}. \tag{2.21}$$

The spin-orbit magnetic field is directed along the axis of the nanotube.

Figure 2.6 shows the spectrum with spin-orbit coupling included. Comparing to Figure 2.5 we see the zero-field degeneracy of 4 is split

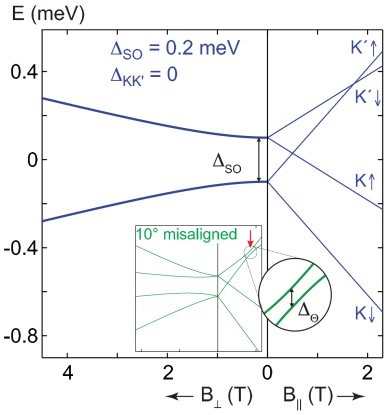

Figure 2.6: Nanotube spectrum including spin-orbit interaction. The nanotube states split according to their combined g-factor as before, but the spin-orbit coupling now acts to align orbital and spin magnetic moments, even at zero field. The zero-field splitting Δ_{SO} motivates the definition of a spin-orbit magnetic field $B_{\mathrm{SO}} = \Delta_{\mathrm{SO}}/g_{\mathrm{s}}\mu_{\mathrm{B}}$. By slanting the magnetic field away from parallel spin-up and spin-down states are mixed as shown by the anticrossing in the inset. Figure adapted from Laird *et al.* [11].

into 2: a pair which has spin and orbital magnetic moments aligned ($K'\uparrow$ and $K\downarrow$) and one that has them anti-aligned. The slopes are the same as before.

Note that the state labels have been removed from the perpendicular part of the spectrum because valley and spin are not good quantum numbers in this case.

The inset shows how misaligning the magnetic field relative to the nanotube axis changes the spectrum. A considerable change is seen in the perpendicular part since the magnetic field now also couples to the orbital motion. For a parallel field the $K'\downarrow$ and $K'\uparrow$ states exhibit an anti-crossing due to their spins being mixed. This gap has a magnitude

$$\Delta_\Theta = |\Delta_{\mathrm{SO}}| \tan\Theta \tag{2.22}$$

where Θ is the misalignment angle.

Disorder in the nanotube Impurities and dislocations are included in the spectrum by a disorder term $\Delta_{KK'}$ which mixes K and K' states with the same spin. It is a phenomenological parameter that is not derived from first principles.

Figure 2.7 shows the spectrum with both spin-orbit coupling and disorder. The crossing of the $K\uparrow$ and $K'\uparrow$ states is now an anti-crossing due to K and K' being mixed. Neither spin nor valley are good quantum numbers.

The complete Hamiltonian Combining the contributions above involves setting up a Hamiltonian in $A-B$ subspace[2] for parallel magnetic field and without disorder and diagonalizing it. While it does provide some physical insight it is outside the scope of this thesis. We simply give the result in the approximation

$$E_{\mathrm{G}}^0 \gg |\Delta_{\mathrm{SO}}^1|, \mu_{\mathrm{orb}}^0 |B_\parallel| \tag{2.23}$$

where μ_{orb}^0 is the orbital magnetic moment of the (electron or hole) shell closest to the band gap. This is justified for typical semiconducting and narrow-gap nanotubes. It does not hold for true metallic nanotubes, though, since they have no band gap.

We will use the definition

$$E_{\tau,s}^{\pm} \approx E_0^{\pm} + s\tau\frac{\Delta_{\mathrm{SO}}}{2} + \left(\mp\tau g_{\mathrm{orb}} + \frac{1}{2}sg_{\mathrm{s}}\right)\mu_{\mathrm{B}}B_\parallel \tag{2.24}$$

where

$$E_0^{\pm} = \pm\sqrt{E_{\mathrm{conf}}^2 + (E_{\mathrm{G}}^0)^2/4} \tag{2.25}$$

and E_{G}^0 is the combined quantization and curvature band gap. The magnetic field is expressed as

$$\mathbf{B} = (B_\parallel, B_\perp) = B(\cos\theta, \sin\theta) \tag{2.26}$$

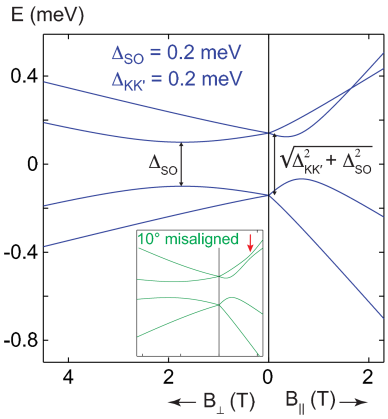

Figure 2.7: Nanotube spectrum including both spin-orbit coupling and disorder. Neither spin nor valley are good quantum numbers if spin-orbit and disorder effects are taken into account. Disorder $\Delta_{KK'}$ causes an anti-crossing of the $K'\uparrow$ and $K\downarrow$ states and also contributes to the zero-field splitting. Figure adapted from Laird *et al.* [11].

[2] Recall that the graphene unit cell contains two inequivalent carbon atoms, A and B.

where θ is the angle between the nanotube axis and the magnetic field. In the basis $(K\uparrow, K'\downarrow, K\downarrow, K'\uparrow)$ we end up with

$$H = \begin{pmatrix} E^{\pm}_{1,1} & 0 & 0 & \Delta_{KK'}/2 \\ 0 & E^{\pm}_{-1,-1} & \Delta_{KK'}/2 & 0 \\ 0 & \Delta_{KK'}/2 & E^{\pm}_{1,-1} & 0 \\ \Delta_{KK'}/2 & 0 & 0 & E^{\pm}_{-1,1} \end{pmatrix} + \frac{1}{2} g_{\mathrm{s}} \mu_{\mathrm{B}} B \begin{pmatrix} 0 & 0 & \sin\theta & 0 \\ 0 & 0 & 0 & \sin\theta \\ \sin\theta & 0 & 0 & 0 \\ 0 & \sin\theta & 0 & 0 \end{pmatrix}. \tag{2.27}$$

Note that in this basis the Hamiltonian is diagonal if no perpendicular magnetic field is applied and no disorder is present. In this case the energies can simply be obtained from (2.24).

The $E_0^{\pm}$ term does not change within a shell. If we define this quantity as the zero of energy for a given shell we should be able to reproduce its spectrum using only the parameters $\Delta_{\mathrm{SO}}, g_{\mathrm{orb}}$, $\Delta_{KK'}$ and the angle of the nanotube axis.

For the $N = 2$ state electron-electron interactions can be included which are sometimes important. Hence, the $N = 2$ states include an additional parameter J for the exchange coupling. We will not discuss the spectrum for $N = 2$ states here, but refer to [13].

2.2 Quantum Dots

In this section we will briefly review the basics of quantum dots before describing cotunneling processes in more detail. The latter will play an important role for data analysis in the Results and Discussion section.

2.2.1 Quantum dot basics

A quantum dot consists of a microscopic region typically of the order of hundreds of nanometers in which electrons are confined by potential barriers. Two requirements are made of the barriers: They must be high enough that the number of electrons is a good quantum number and they must not be so high as to prevent tunneling altogether.

In the following we will use the constant interaction model for the quantum dot. The energy of the quantum dot E is determined by the number of electrons on the dot N, the voltages and capacitances of nearby gates V_i, C_i and the energies of the quantum mechanical levels ϵ_i

$$E = \frac{1}{2C}\left(-|e|(N - N_0) + \sum_i C_i V_i\right)^2 + \sum_i^N \epsilon_i \tag{2.28}$$

where C is the self-capacitance of the dot, typically approximated by $C = \sum_i C_i$.

Using E we can get an expression for the addition energy E_{add}, i.e., the energy for adding an electron given N electrons already on the dot:

$$\begin{aligned} E_{\text{add}} &= \mu_{N+1} - \mu_N = (E_{N+1} - E_N) - (E_N - E_{N-1}) \\ &= \frac{e^2}{C} + \Delta E \equiv U + \Delta E \end{aligned} \tag{2.29}$$

where μ_N is the chemical potential for adding the N'th electron. The charging energy U and the level spacing ΔE are key quantities for the quantum dot.

We can approximate these quantities specifically for a nanotube: The capacitance should be linear in L if the nanotube is much longer than it is wide. Thus, the charging energy can be estimated for a nanotube of length L by making the crude assumption

$$C \approx \epsilon_0 \epsilon_{\text{r}} L \tag{2.30}$$

so that

$$U \approx \frac{e^2}{\epsilon_0 \epsilon_{\text{r}} L} \approx \frac{4.5\,\text{meV}}{L[\mu\text{m}]}. \tag{2.31}$$

where we have used the SiO_2 value for ϵ_{r} of 4.

The level spacing is only added to the charging energy when a longitudinal level in the dot is filled. In the simplest case the energy of the longitudinal levels is simply given by a particle-in-a-box calculation. Taking $E(k_\parallel) = \hbar v_{\text{F}} k_\parallel$ for a Dirac cone and $k_{\parallel,n} = n\pi/L$ for a 1D particle in a box with hard-wall boundary conditions we get

$$\Delta E = \hbar v_{\text{F}} (k_{\parallel,n} - k_{\parallel,n-1}) = \frac{h v_{\text{F}}}{2L} \approx \frac{1.7\,\text{eV}}{L[\mu\text{m}]} \tag{2.32}$$

Longitudinal levels are often called shells to emphasize the similarity between quantum dots and atoms. As discussed in the previous section carbon nanotube shells are four-fold degenerate in contrast to most other system[3] which only exhibit two-fold degeneracy.

[3] E.g., nanowires, 2-dimensional electron gases etc.

2.2.2 Transport in a quantum dot

To describe transport through the quantum dot we define the Hamiltonian H for the system consisting of a dot and two metal leads

$$H = H_{\text{D}} + H_{\text{L}} + H_{\text{R}} + H_{\text{T}} \tag{2.33}$$

where the first three terms determine the energy levels of the dot and the left and right leads. We denote this non-interacting part of the Hamiltonian by H_0. The last term is the transfer term which transfers

electrons between the leads and dot. It can be split into parts concerning either lead

$$H_{\mathrm{T}} = H_{TL} + H_{TR} \tag{2.34}$$

Transport through the quantum dot can be described by using a transfer matrix T which is given self-consistently as [14]

$$T = H_T + H_T \frac{1}{E_i - H_0} T \tag{2.35}$$

where E_i is the energy of the initial state.

The transition rate of electrons $\Gamma_{\beta\alpha}$ from state α to state β is then given by

$$\Gamma_{\beta\alpha} = \frac{2\pi}{\hbar} \left|\langle\beta| T |\alpha\rangle\right|^2 \delta(E_\beta - E_\alpha) \tag{2.36}$$

where the delta function δ ensures energy conservation. Sequential tunneling is the first-order contribution to this rate. Take, for instance, the first-order term of the rate for the transition between α and β which moves one electron from the left lead onto the dot:

$$\Gamma^{\mathrm{1st,L}}_{\beta\alpha} = \frac{2\pi}{\hbar} \left|\langle\beta| H_{TL} |\alpha\rangle\right|^2 \delta(E_\beta - E_\alpha) \tag{2.37}$$

To transport an electron from the left lead to the right lead we need two of the above processes: left lead $\rightarrow$ dot and dot $\rightarrow$ right lead. That is, transport occurs in separate steps. This is shown in Figure 2.8.

Sequential tunneling is also possible through excited states as shown in panel 4 in the same figure.

If only sequential tunneling is considered a current can only flow when the chemical potential of a transition (say, $\mu_{N\leftrightarrow N+1}$ from N to $N+1$) is positioned between the Fermi energy of the leads:

$$\mu_L > \mu_{N\leftrightarrow N+1} > \mu_R. \tag{2.38}$$

Transitions that are between the chemical potentials of the two leads are said to be in the bias window. In this situation the dot occupation oscillates like $N \rightarrow N+1 \rightarrow N$. If no transition satisfies this condition no current flows, i.e., the dot is in Coulomb blockade.

Cotunneling is the second-order contribution to $\Gamma_{\beta\alpha}$. Second-order processes transport electrons all the way from the left to the right lead[4]. Consider a second-order process that takes an electron from the left lead and puts it in the left lead via the intermediate state $H_{TL}|\alpha\rangle$.

$$\Gamma^{\mathrm{2nd}}_{\beta\alpha} = \frac{2\pi}{\hbar} \left|\langle\beta| H_{TR} \frac{1}{E_\alpha - H_0} H_{TL} |\alpha\rangle\right|^2 \delta(E_\beta - E_\alpha) \tag{2.39}$$

Here, the states α and β differ by one electron in the leads.

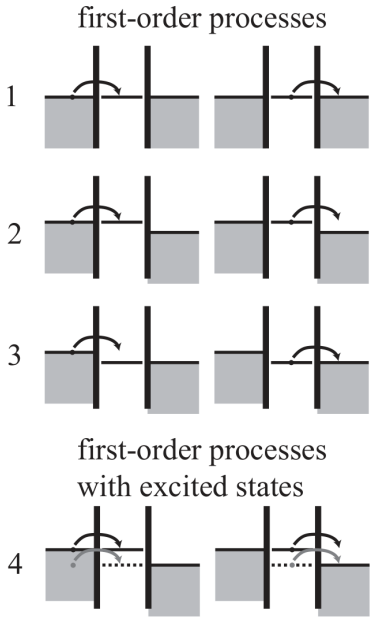

Figure 2.8: Sequential tunneling in a quantum dot. This type of transport is first-order in the lead couplings Γ_i and is only possible when a transition in the dot is in the bias window defined by the leads. **(1)-(3)** Transporting an electron across the dot requires two sequential tunneling events. **(4)** By increasing the bias window excited states can also be used for transport. Adapted from Ihn [15].

[4] They may also transport electrons from a lead onto the dot and then into the initial lead again, but these processes do not contribute to the current.

Cotunneling processes are shown in Figure 2.9. They are either elastic or inelastic: In elastic cotunneling the initial and final state of the dot have the same energy, i.e. an electron transfers onto the dot and the same electron tunnels out again. In inelastic cotunneling an electron is removed from a level that is different from the one that was tunneled into by the first electron. In the latter case the energy difference between the initial and final state of the dot is provided by, e.g., the source-drain voltage or microwave radiation. In this project we will only consider source-drain voltage as the energy provider for cotunneling.

Let's rewrite (2.39) a bit to gain some intuition. Letting H_0 act on $|\alpha'\rangle \equiv H_{TL}\,|\alpha\rangle$ gives $E_{\alpha'}$ so the fraction above becomes

$$\frac{1}{E_\alpha - H_0}\,|\alpha'\rangle = \frac{1}{E_\alpha - E_{\alpha'}}\,|\alpha'\rangle \tag{2.40}$$

The transfer Hamiltonians $H_{L,R}$ contain the tunneling amplitudes $t_{L,R}$ between the leads and the dot, so, leaving out the details, $\Gamma^{\text{2nd}}_{\beta\alpha}$ becomes

$$\Gamma^{\text{2nd}}_{\beta\alpha} \propto \frac{|t_{\text{R}}|^2|t_{\text{L}}|^2}{(E_\alpha - E_{\alpha'})^2} \tag{2.41}$$

The quantity $E_\alpha - E_{\alpha'}$ is the difference between the initial configuration and the configuration in which one electron in moved from the lead onto the dot. If state α has N electrons on the dot this energy difference is

$$E_\alpha - E_{\alpha'} = \epsilon_L - \mu_{N+1} \tag{2.42}$$

where ϵ_L is the energy of the electron in the lead that was transferred.

Let's restate (2.41) as[5]

$$\frac{|t_{\text{R}}|^2|t_{\text{L}}|^2}{(\epsilon_L - \mu_{N+1})^2} \propto \frac{\tau^2_{\alpha'}}{\tau_R \tau_L} \tag{2.43}$$

This fraction sets the amplitude for the cotunneling process. In order to have an appreciable amplitude $\tau_R\tau_L$ should be of the same order or smaller than $\tau^2_{\alpha'}$. Intuitively this means that the electron must be able to tunnel through the left and right barriers in a time comparable to or smaller than the time $\tau_{\alpha'}$ it's allowed to be in the virtual state α'. Thus, cotunneling is expected to be stronger in dots with strong tunnel couplings.

Elastic cotunneling is only limited by the amplitude (2.43) so it can occur even when the dot is in Coulomb blockade. Inelastic cotunneling has the further limitation that the source-drain voltage must match the energy difference between two levels in the quantum dot. Thus, when the current is dominated by cotunneling (i.e., in Coulomb blockade) *the current increases sharply when the source-drain voltage matches the energy difference between two energy levels in the dot.* Using this property of cotunneling to gain knowledge about the spectrum of the dot is called

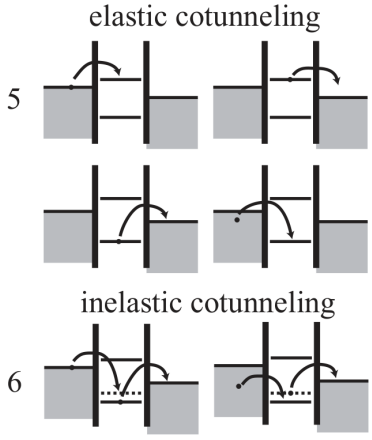

Figure 2.9: Cotunneling in a quantum dot. These second-order processes transport an electron across the dot via an intermediate state with a classically forbidden energy. **(5)** In elastic cotunneling processes the initial and final energy of the dot are the same, although the state of the dot electrons need not be. **(6)** If the final and initial states of the dot do not have the same energy the process is inelastic. The extra energy must be provided from somewhere else, in this case the source-drain bias. Adapted from Ihn [15].

[5] We're using $|t|^2 \propto 2\pi|t|^2 d = \Gamma \sim h/\tau$ where d is the density of states which is assumed constant. In a rigorous treatment the density of states is obtained from integration over initial and final states. $\tau_{\alpha'} = h/(\epsilon_L - \mu_{N+1})$ is the characteristic time that the system is allowed to virtually occupy the intermediate state α'.

excitation spectroscopy. We will use this technique to determine the parameters of the nanotube in the Results and Discussion section

The condition above also means that no inelastic cotunneling current is possible before $|e|V_{\rm SD}$ is equal to the energy difference between the lowest two levels in the dot Δ_1. For $|V_{\rm SD}| > \Delta_1/|e|$ the current depends linearly on source-drain bias because increasing $V_{\rm SD}$ allows more states in the leads to participate in the transport.

Finally, when the leads are superconducting and not metallic we should take into account the superconducting gap $\Delta_{\rm SC}$ and the fact that the superconducting density of states is different from that in a metal. In the absence of in-gap states no transport is allowed before the source-drain bias is raised above $\Delta_{\rm SC}$ since no quasiparticle states are available in the leads. This superconducting density of states may change the magnitude of the inelastic cotunneling current, but we will not consider such effects here.

2.2.3 Kondo physics in a quantum dot

The conventional Kondo effect arises from a magnetic impurity embedded in a metal [16]. Conduction electrons interact with the spin of the impurity and form a many-body state with a characteristic energy $k_{\rm B}T_{\rm K}$. This causes scattering between conduction electrons and increases the resistance once the temperature drops below $T_{\rm K}$.

A quantum dot with an odd number of electrons has a net spin-$\frac{1}{2}$. The occupied state with the highest energy will be doubly degenerate if time-reversal symmetry is not broken. We can now imagine cotunneling processes like above in which the dot electron with, say, spin up tunnels out and a conduction electron with spin down tunnels in. The net result is a spin flip of the dot electron. Combining all processes of this type again results in a many-body "Kondo" state between conduction electrons in the lead and the dot electron. Rather than suppress current as in a metal the Kondo state actually enhances current since it provides a spatially extended state at zero bias. For a degeneracy of 2 this effect is known as the SU(2) Kondo effect which again has a characteristic energy of $T_{\rm K}$ (if we drop the $k_{\rm B}$). Its effect is to increase the conductance at zero bias to a maximum of $2e^2/h$ rather than the standard e^2/h for sequential transport through a single level. The Kondo effect is only observed when the lead couplings are large since it involves cotunneling processes.

We can imagine the same processes in a carbon nanotube, but in this system the level degeneracy is four rather than two. If the carbon nanotube levels are not too split relative to the lead couplings we get the SU(4) Kondo effect which involves all four levels. This naturally gives rise to a maximum conductance at zero bias of $4e^2/h$. Thus, depending

on the value of the lead couplings we can observe both the SU(2) and SU(4) Kondo effect in a carbon nanotube.

Chapter 3

Fabrication and Experimental setup

3.1 Fabrication

Device fabrication on the nano scale requires use of multiple advanced techniques, all of which have a number of tunable parameters that must be just right in order for the fabrication to be successful. Part of the present project has been to figure out the right combination of parameters for the fabrication of carbon nanotube devices with arbitrary geometries, i.e. figuring out the fabrication recipe. An overview of this development process as well as the final recipe are available in Appendix A.1.

The general fabrication goal was carbon nanotube devices with arbitrary geometries and specifically devices with Cooper pair splitter (CPS) geometries. One such device is shown in Figure 3.1. The CPS geometry consists of a central superconducting lead with two normal leads placed symmetrically on either side of it. The side gates can be on either side of the nanotube. This geometry defines two quantum dots in the carbon nanotube that can be tuned with the side gates. Several of such devices have been fabricated in this project but all the data presented in this thesis is taken for the device shown in Figure 3.1 which will be called devA in this work (in fabrication it is known as `cnt_gen5_FI`).

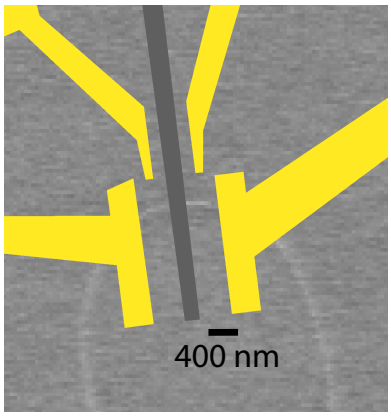

Figure 3.1: Scanning electron microscope (SEM) image of the nanotube in devA with metal leads overlaid digitally. The gold areas are 50 nm Au and the dark grey area is 5/15 nm Ti/Al. The image was taken before metal leads were deposited which is why they are overlaid instead. To avoid the risk of damaging the nanotube no SEM image has been taken of the device after metal leads were deposited.

The normal (i.e., non-superconducting) leads on devA consist of 50 nm Au (thermal evaporation). Typically, a thin layer (~ 5 nm) of titanium or chromium is deposited below the Au to "stick" the Au to the surface of the chip since Au peels off easily by itself. Due to fabrication irregularities this sticking layer was not deposited on devA which means that the nanotube is in direct contact with the Au.

The superconducting lead on devA is 5/15 nm Ti/Al (e-beam evaporation). A thin layer was chosen for the aluminium to give a high critical

in-plane field in the superconducting state. The standard value for the critical magnetic field of bulk aluminium at 0 K is 10.5 mT [17]. This value is too low to change the energy levels in a typical carbon nanotube appreciably which is required for the Braunecker proposal.

One concern about the fabrication process was the necessity of imaging the carbon nanotubes with a SEM after growth in order to design device geometries on them. We were concerned that SEM electron beam would damage the nanotubes and alter its electronic properties. Although several devices with carbon nanotubes of high quality have been fabricated in this project it is unknown whether the yield would have been higher if the nanotubes had not been imaged. It is the impression of this author, though, that the adverse effects of imaging are negligible compared to the type of metal used in the leads, the width of the metal leads, and how well resist is removed in the development step before depositing metal leads.

3.2 Experimental Setup

All measurements were done in a Oxford Instruments Triton200 dilution refrigerator at a base temperature of 34 mK unless otherwise specified. The base temperature is calibrated at installation by Oxford Instruments engineers using ^{60}Co nuclear orientation thermometry. During standard operation the base temperature is measured using a RuO_2 sensor. The electron temperature was not measured in this project but it is typically ~ 100 mK.

Temperatures in the tens of millikelvins range are achieved by dilution refrigerators by letting ^{3}He cross a phase boundary between a pure ^{3}He phase (the concentrated phase) and a ^{3}He-^{4}He phase (the dilute phase). In doing so the ^{3}He extracts energy from the system. This process occurs continuously in a mixing chamber. Pumping on the dilute phase preferentially removes ^{3}He which prevents the phases in the mixing chamber from reaching equilibrium. The ^{3}He is then recycled and eventually enters the concentrated phase again where the process is repeated.

The Triton200 refrigerator is cryogen free, meaning that the ^{3}He-^{4}He mixture is kept in a closed loop. Having a closed loop is advantageous because liquid ^{4}He and especially ^{3}He are rather expensive.

The refrigerator is fitted with a superconducting vector magnet powered by a Mercury iPS. The magnet can reach (nominally) 3 T in the x-direction and 8.5 T in the z-direction. The magnet is unable to set a field in the y-direction. Cylindrical polar coordinates can also be used which allows the magnetic field to be set at an arbitrary angle within (nominally) 3 T in the x-z plane.

The electrical setup is as shown in Figure 3.2. All DC lines in the

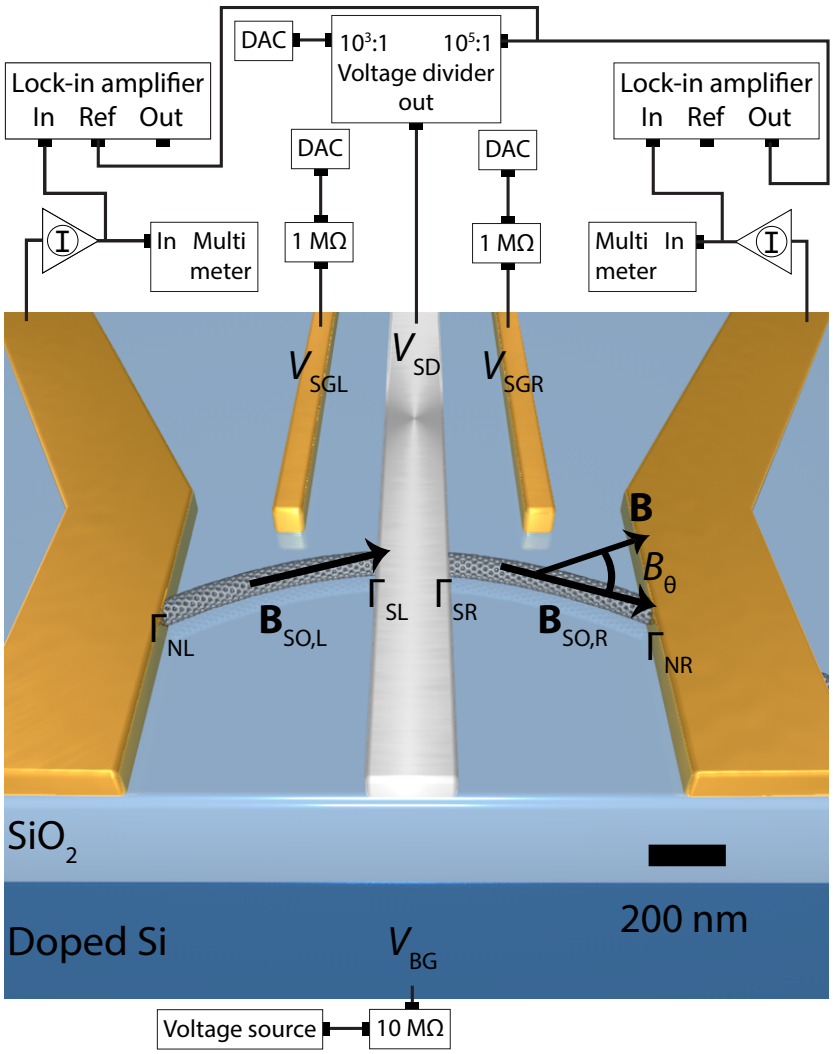

Figure 3.2: Setup for measuring devA. A DC+AC bias is applied to the central superconducting lead and the corresponding DC+AC current through each nanotube segment is measured two-terminally. Couplings Γ_i, magnetic field $\mathbf{B}$ and spin-orbit magnetic fields $\mathbf{B}_{\mathrm{SO,i}}$ are shown on the device. The global angle B_θ is measured from an extracted average of the shells in the right segment. The makes of the instruments is specified in the main text.

cryostat go through an RF filter to prevent high frequency noise. All lines also go through an RC filter for low-frequency filtering, but only the lines connecting the side gates have resistances in the RC filter. For the remaining lines the resistance was removed from the RC filter to make correlation measurements easier. The specific instrument models used are as follows: DAC: DecaDAC custom-built by Jim MacArthur at Harvard. Lock-in amplifiers: Stanford Research Systems SR830. Multimeters: Agilent 34401A. Current amplifiers: Ithaco DL1211. Voltage source: Keithley 2614B.

The figure also shows the couplings between the normal leads and the nanotube Γ_{NL} and Γ_{NR}, and the coupling between the superconducting lead and the nanotube Γ_{SL} and Γ_{SR}.

Note that the magnetic field $\mathbf{B}$ is constrained to the plane of the

device so that B_θ is also in the plane of the device.

The current amplifier has two inequivalent output connections. One which passes the signal through a low-pass filter with a variable time constant and one in which the signal is not filtered. The first output is configured to a time constant of $\sim 100\,\mathrm{ms}$ and sent to a multimeter for measuring DC current. The second signal is sent to a lock-in amplifier for measuring differential conductance using standard techniques.

The differential conductance $\mathrm{d}I/\mathrm{d}V_\mathrm{SD}$ is obtained using either the lock-in signal or numerically differentiated DC current which is in some cases less noisy. The second derivative of the current $\mathrm{d}^2I/\mathrm{d}V_\mathrm{SD}^2$ is always obtained by numerically differentiating the lock-in signal by V_SD.

Data acquisition was done with the matlab-qd framework for Matlab written by Anders Jellinggaard[1].

[1] The framework is available here `https://github.com/qdev-dk/matlab-qd`. Special thanks go to Anders for supplying this code which simplified data acquisition immensely.

Chapter 4

Results and Discussion

In this section we will present data from devA and assess its utility as a CNT-CPS based on the requirements given in the introduction. We measure devA as two quantum dots in parallel as shown in Figure 3.2: A bias V_{SD} is applied to the superconducting lead and the normal leads are grounded. We will use "dot" and "side" interchangeably to refer to the nanotube segments on either side of the superconductor. Measurements are done at 34 mK unless otherwise noted.

Non-local conductance measurements on devA have been conducted but since they are inconclusive they are not presented here.

4.1 Basic characterization

Room temperature gate traces for the left and right side are shown in Figure 4.1. The traces are taken in vacuum at a pressure of about 1×10^{-3} mbar. From the dip in conductance at $V_{BG} \approx 0$ V we expect the nanotube to have a narrow gap. The right side conductance has a hysteretic, but perfectly symmetric behavior when sweeping the gate in opposite directions.

Figure 4.2 shows bias spectroscopy plots at 34 mK of the left and right sides of devA. The plots do not show the same backgate range, but are zoomed in on the shells that will be analyzed later. The 4-fold symmetry characteristic of carbon nanotube quantum dots is clearly visible.

Naming of the shells is indicated at the top of the plots with lowercase (uppercase) letters counting down (up) for increasing backgate voltage. In the left side the letter numbering starts at the first shell which shows a minimum of Coulomb blockade. Shells at higher backgate voltages than this are not Coulomb blockaded but exhibit conductance fluctuations that do not go to zero anywhere. In the right side the letter numbering starts at the best guess for the band gap (the position of the band gap is discussed below). Note that some shells, e.g. shell O, can be referred to

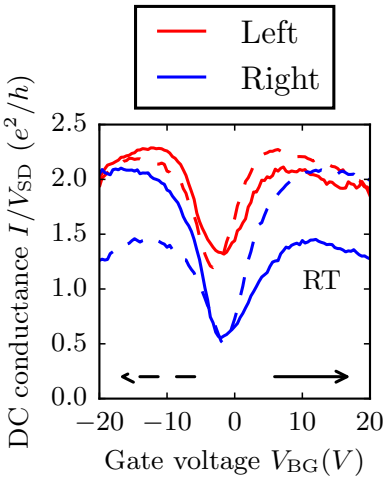

Figure 4.1: Room temperature DC conductance as a function of backgate voltage V_{BG} for devA. This measurement was conducted in a probe station by DC-biasing one lead with $V_{SD} = 10$ mV and grounding another by using probe needles. Thus, the setup is much simpler than shown in Fig 3.2 and the nanotube segments are not measured in parallel. The right side is very hysteretic, but also remarkably symmetric in its hysteresis. The dips in conductance around $V_{BG} \approx 0$ would generally be interpreted as indicating the presence of a band gap in the nanotubes.

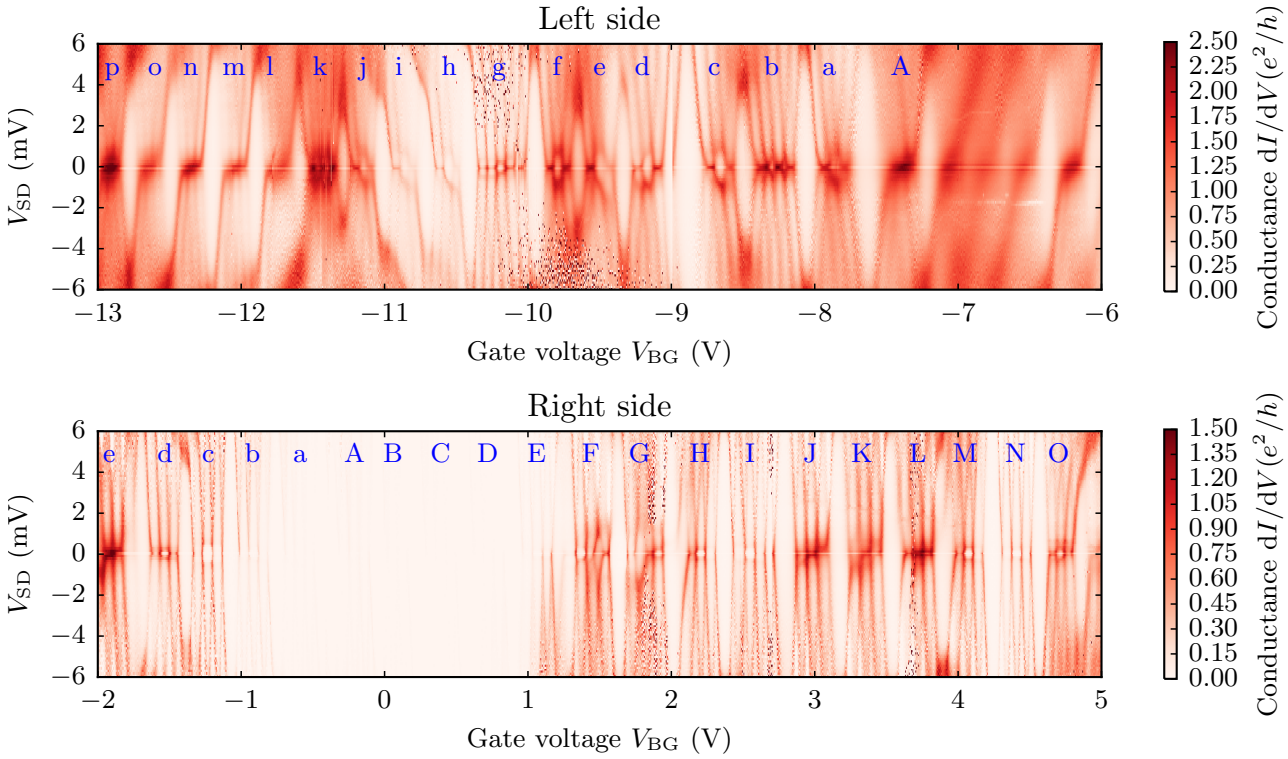

Figure 4.2: Bias spectroscopy of devA. Both sides show clear 4-fold symmetric behavior characteristic of carbon nanotubes. The lead couplings are generally stronger in the left side as indicated by higher conductance and Kondo resonances. Letters show the naming of the shells. Note that the backgate range is different for the two sides. However, the size of the range is the same so widths are comparable in the two plots.

without specifying which side they are in because they are only defined in one side.

In order to do the entanglement measurement in the Braunecker proposal we must use a shell from each side. It is convenient that these shells are not too far from each other in V_{BG} since the side gates are limited in how much they can tune the dots individually. This was not possible in devA because the left side is not sufficiently Coulomb blockaded for $V_{BG} > -6\,V$. It still shows a regular electronic structure but the shells are too strongly coupled. In the right side the shell structure becomes gradually more disordered at negative V_{BG} so we can't use those shells either.

Some shells appear to consist of 5 or 6 peaks rather than 4, e.g., left shells b and g and right shells F and I. In the left side this is typically caused by switching[1]. The shells in the right side do not have obvious switches. Shells F and G also appear less symmetrical than, say, shell J. These two observations could be an indication that the electronic structure of some shells on the right side is disturbed by disorder.

What appears to be the band gap in the right side between $V_{BG} = -1$ and $1\,V$ is actually a weakly coupled region. It is shown in more detail in Figure 4.3. In fact, the band gap is not easily identifiable in either side, probably because it has about the same magnitude as the

[1] A switch denotes the situation where the voltage felt by the nanotube changes abruptly although all user-controlled voltages are varied continuously. It can be caused by, e.g., charge traps.

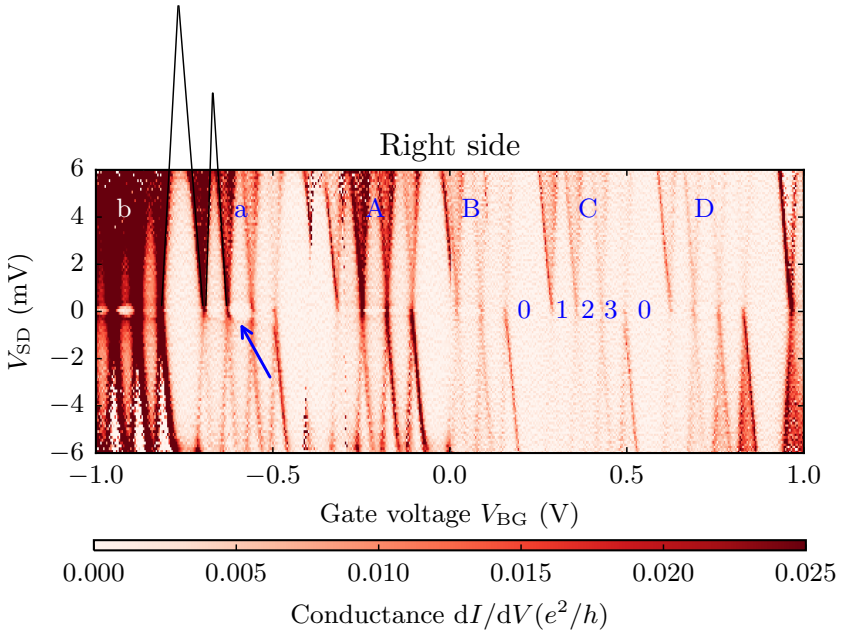

Figure 4.3: Zoom in of bias spectroscopy plot in the weakly coupled region around $V_{\mathrm{BG}} \approx 0$. What appears to be a band gap in the previous figure is shown to be a weakly coupled region in this plot. The larger coulomb diamond between shells a and A can be conjectured to represent a band gap, although its size may just as well be caused by a switch. The numbers in shell C is indicates the filling. An arrow denotes the onset of inelastic cotunneling with its characteristic circular appearance in shell a. Addition energies for $N = 0$ and $N = 1$ fillings in shell a are indicated by lines.

charging energy. The largest separation between two shells in the weakly coupled region is between shells a and A. This was chosen as the best guess for the band gap and the zero-point for numbering with the hope that lowercase shells would correspond to holes exclusively. Due to its small magnitude and the conductance feature inside it, this gap is not convincing as a band gap, though. Also, there is no band gap at this backgate position on the left side. These observations mean that we can't make the unambiguous identification about holes above.

Also shown in Figure 4.3 is the occupation within shell C. The occupation is specified as N mod 4. In the following we will mean N mod $4 = a$ when we write the occupation as $N = a$ except when we describe a filled shell explicitly as $N = 4$. When the dot is not Coulomb blockaded the filling oscillates which is specified as $N = a \leftrightarrow a + 1$. In shell A in the same figure an arrow shows the position of onset of inelastic cotunneling current which is most prominent as a circular feature at $N = 2$ occupation.

We can find the charging energies U_{L}, U_{R} and the level spacings ΔE_{L}, ΔE_{R} from the bias spectroscopy. For the right side this is most easily done in Figure 4.3 because the Coulomb diamonds are clearer here. We obtain

$$U_{\mathrm{R}} \approx 9\,\mathrm{meV}, \qquad \Delta E_{\mathrm{R}} \approx 4\,\mathrm{meV}.$$

The left side charging energy is harder to extract due to the Kondo

resonances. We estimate $U_{\mathrm{L}} \approx 6\,\mathrm{meV}$ and

$$U_{\mathrm{L}} \approx 6\,\mathrm{meV}, \qquad \Delta E_{\mathrm{L}} \approx 0 - 4\,\mathrm{meV}.$$

The left side level spacing does show variation, almost going to zero between shells f and e. The varying levels spacings mean that the particle-in-a-box approximation is not accurate and they indicate that the potential landscape is disordered.

Rough estimates for U and ΔE for dots with $L = 0.4\,\mu\mathrm{m}$ are

$$U_{\mathrm{est}} \approx \frac{4.5\,\mathrm{meV}}{L[\mu\mathrm{m}]} \approx 11\,\mathrm{meV}, \qquad \Delta E_{\mathrm{est}} \approx \frac{1.7\,\mathrm{meV}}{L[\mu\mathrm{m}]} \approx 4\,\mathrm{meV} \tag{4.1}$$

valid for both left and right side since they have the same nominal length. The estimates agree reasonably well with our measurements. The larger estimated U_{est} can be attributed to the crudeness of our assumption for the capacitance.

Given the lower charging energy in the left dot we would expect it to be larger than the right dot. Since the coupling to at least one of the leads is always strong in the left side the wave function on the dot must have a sizable overlap with the strongly coupled lead. Thus, the effective size of the dot is larger than in a situation where the wave function is concentrated in the middle of the nanotube segment. Even with this argument the size of the dot should not be more than $0.4\,\mu\mathrm{m}$, though.

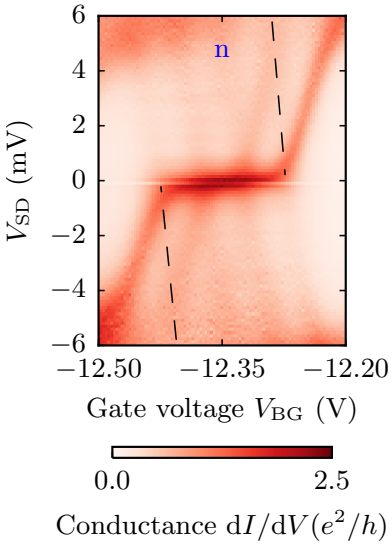

Figure 4.4: Bias spectroscopy zoom of shell n. The diagonal lines in the data are caused by a strongly asymmetric coupling while the horizontal line is an SU(4) Kondo resonance. Dashed lines indicate the additional lines that would be expected in the absence of a Kondo resonance.

4.2 Asymmetric couplings

A prominent feature on the left side is the difference in intensity between conductance resonances at positive and negative bias. For instance, in shell n (see Figure 4.4 and disregard the dashed lines for now) the conductance for $N = 0$ is higher for $V_{\mathrm{SD}} < 0$ than for $V_{\mathrm{SD}} > 0$. For $N = 4$ the situation is opposite. The overall visual effect is a diagonal line on either side of the shell. These diagonal features can be explained by a very large or very small coupling asymmetry $\Gamma_{\mathrm{NL}}/\Gamma_{\mathrm{SL}}$ by the following argument:

Consider a negatively biased ($V_{\mathrm{SD}} < 0$) quantum dot with two normal leads[2] as in Figure 4.5. Assume that the level splitting of the four levels in a nanotube shell is smaller than V_{SD} and that the dot chemical potential is tuned so that four levels are in the bias window. For a filling of $N = 0 \leftrightarrow 1$ the rate of transfer for an electron tunneling from the left lead to the dot is $4\Gamma_1$ since there are four levels to tunnel into. The rate of transfer for tunneling from the dot into the right lead is just Γ_2 since no more than one state can be occupied at a time. Now, using the typical estimate for the height of the Coulomb peaks in a quantum dot [15]

$$I \propto \frac{4\Gamma_1\Gamma_2}{4\Gamma_1 + \Gamma_2} \approx 4\Gamma_1 \tag{4.2}$$

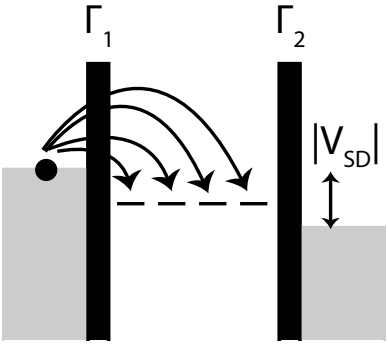

Figure 4.5: Schematic of an electron tunneling into a quantum dot with four degenerate levels. If the levels all have the coupling Γ_{S} to the lead the overall transition rate for the electron will be $4\Gamma_1$. Once the electron is on the dot the transition rate for going into the right lead is just Γ_2. The situation is reversed for opposite bias.

[2] The same argument can be made for a superconducting lead by simply taking into account that all features are pushed away from zero bias by the superconducting gap Δ_{SC}.

where the approximation is made for $\Gamma_1 \ll \Gamma_2$. Similarly, if the bias is reversed then the rate for tunneling from the right lead onto the dot includes the factor of 4 and we get

$$I \propto \frac{\Gamma_1 4\Gamma_2}{\Gamma_1 + 4\Gamma_2} \approx \Gamma_1 \tag{4.3}$$

which is a factor of 4 smaller than in the first case. Thus, if the lead couplings are very dissimilar (their ratio is far away from 1) and the dot has degenerate levels the current will differ by the degeneracy on reversing the bias. As the shell is filled the degeneracy factors for positive and negative bias change. For $N = 4$ filling they are switched completely compared to the $N = 0$ case which means that that maximum current now occurs for the opposite sign of V_{SD}.

In short, the conductance at $N = 0$ will be highest (lowest) at positive V_{SD} if the coupling to the source lead (always the superconductor in our case) is much stronger (weaker) than the coupling to the drain lead.

With this argument we would expect the dashed lines in Figure 4.4 to be as strong as the diagonal conductance lines in the data. This discrepancy can be explained by the presence of Kondo resonances which are explained below. The presence of Kondo resonances does not change the conclusion of the argument above. Note that the shells in Figure 4.3 exhibit the expected diagonal pattern caused by asymmetric coupling since no Kondo resonances are present in these shells.

We can now deduce the coupling asymmetry in shells with diagonal lines. We observe a strong coupling dependence on V_{BG} in the left side. For instance, the coupling asymmetry changes from $\Gamma_{\mathrm{NL}}/\Gamma_{\mathrm{SL}} \gg 1$ in shells o, n, m, l to $\Gamma_{\mathrm{NL}}/\Gamma_{\mathrm{SL}} \ll 1$ in shells j, i, h. The right side generally has coupling asymmetries closer to unity. In the weakly coupled region around $V_{\mathrm{BG}} = 0$ we do see $\Gamma_{\mathrm{NR}}/\Gamma_{\mathrm{SR}} \ll 1$, though.

4.3 Kondo physics

Kondo resonances are visible in many shells, e.g., O and f. They are visible as resonances at zero bias for odd occupations of the dot. In some shells, notably o, n, m, l, the coupling to the leads is so strong that the Kondo resonance involves all four nanotube level. In this case the conductance increases beyond $2e^2/h$.

For our purposes this is not ideal. The Braunecker proposal requires well-resolved spin states and the Kondo state is exactly a *mixture* of spin states with the lead electrons. Also, it impedes excitation spectroscopy measurements since the conductance due to the Kondo effect dominates that due to inelastic cotunneling.

In shells with Kondo resonances the current onset at the edges of the $N = 1, 2, 3$ Coulomb diamonds is not obvious because at these points

the current is almost at its maximum value already at $V_{\mathrm{SD}} \approx 0$. Contrast this with, e.g., shell a in the right side (Figure 4.6) which is more weakly coupled and does not have Kondo resonances. In this shell the edges of the $N = 1, 2, 3$ Coulomb diamonds are more clearly visible. The asymmetric coupling effect is more clearly seen to be reversed in bias, although the negative bias conductance is generally lower than at positive bias. The asymmetric coupling argument does not account for this.

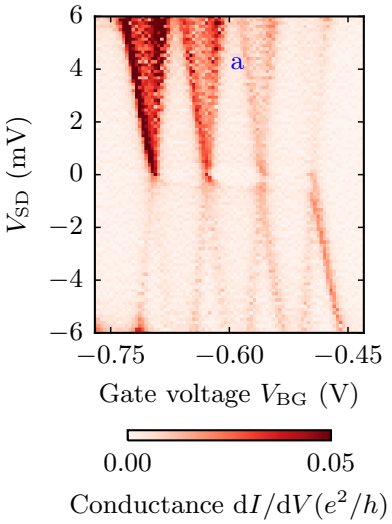

Figure 4.6: Bias spectroscopy zoom of shell a (right side). Due to the absence of a Kondo resonance this shells shows more clearly that the current is asymmetric on reversing the bias as expected for strongly asymmetric lead couplings.

4.4 Superconducting features

Figure 4.7 shows bias spectroscopy of six specific shells at both medium and low bias. In the latter plot the superconducting gap is visible as the middle region in which the Coulomb peaks change character and become curved. This effect is more obvious in the left dot which indicates that it is more strongly coupled to the superconductor than the right dot. We can estimate the superconducting gap at about 60 µeV as the point in bias where the Coulomb peaks become vertical. Resonances inside the superconducting gap correspond to transport via Andreev reflections or Shiba states.

4.5 Parameter estimation

To find the parameters for the nanotube we use inelastic cotunneling spectroscopy. Fixing the backgate value in the middle of a Coulomb diamond we sweep V_{SD} and step the magnetic field strength or angle. Abrupt increases in the differential conductance $\mathrm{d}I/\mathrm{d}V_{\mathrm{SD}}$ occurs when $|e|V_{\mathrm{SD}}$ is equal to the energy difference between two levels. These increases show up as peaks or dips in $\mathrm{d}^2I/\mathrm{d}V_{\mathrm{SD}}^2$. Energy level differences are calculated using (2.27) and overlaid on the cotunneling data. The parameters are fitted manually until correspondence with the data is achieved.

A total of 10 shells have been measured as a function of magnetic field oriented (approximately) parallel and perpendicular to the nanotube axis and as a function of magnetic field angle at $B = 2\,\mathrm{T}$.

We introduce the global B_θ angle which measures angles relative to the average of the shell angles on the right side (see Figure 3.2). This quantity is useful for comparing angles between shells and between the left and the right side. The angle θ has the same meaning as in (2.27). Note that the zero-point of θ is a parameter in itself and thus changes from shell to shell.

One representative and well-behaved shell from each side is shown in Figures 4.8 and 4.9 (shells h and N) while the rest are shown in the appendix. The fitted parameters for all shells are shown in Table 4.1

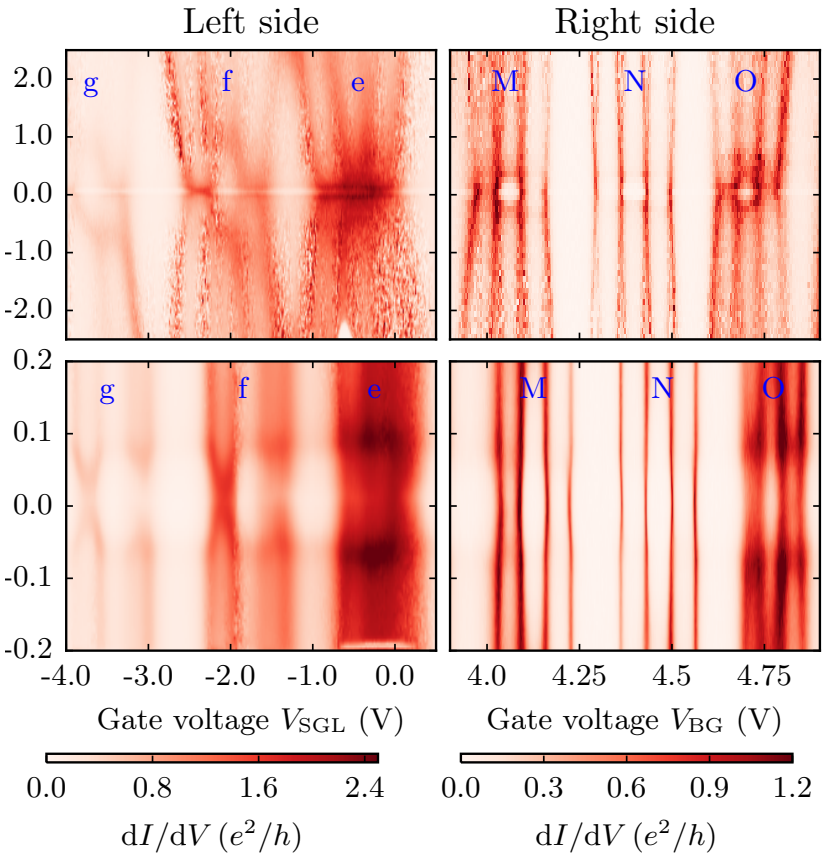

Figure 4.7: Bias spectroscopy at medium and low bias voltages. The superconducting gap is visible in the top row as a narrow line around $V_{\mathrm{SD}} = 0$. In the zoom-in in the bottom row we can read off the value of the gap of about $\Delta_{\mathrm{SC}} \approx 60\,\mu\mathrm{eV}$ (taking bias offset into account).

and plots of the parameters with uncertainties are shown in Figure B.9 in the appendix.

Figure 4.8 shows cotunneling spectroscopy in shell h. This shell is dominated by disorder, i.e., $\Delta_{KK'} > \Delta_{\mathrm{SO}}$ which is true for all four shells in the left side. In the right side the shells generally have less disorder and larger spin-orbit values. These two regimes yield qualitatively different spectra. In particular, the parallel sweeps for $N = 1$ and $N = 3$ are very different for spin-orbit dominated shells while they are almost identical in the disorder dominated case. The spin-orbit values are comparable to what has been found previously [8–10, 18–20], except for the anomalously large values found by Steele *et al.* [21].

From (2.21) we calculate $B_{\mathrm{SO,L}} \approx 0.6 - 1.2\,\mathrm{T}$ and $B_{\mathrm{SO,R}} \approx 1 - 1.6\,\mathrm{T}$. These spin-orbit magnetic fields are about the same as the in-plane critical field of the superconductor of $B_{\mathrm{C}} \approx 0.6 - 0.8\,\mathrm{T}$ which is required by the Braunecker proposal.

Generally, the correspondence between data and theory is excellent. One transition which is predicted by theory but is not observed is the top (and bottom) transition for the $N = 2$ sweeps. This can be explained

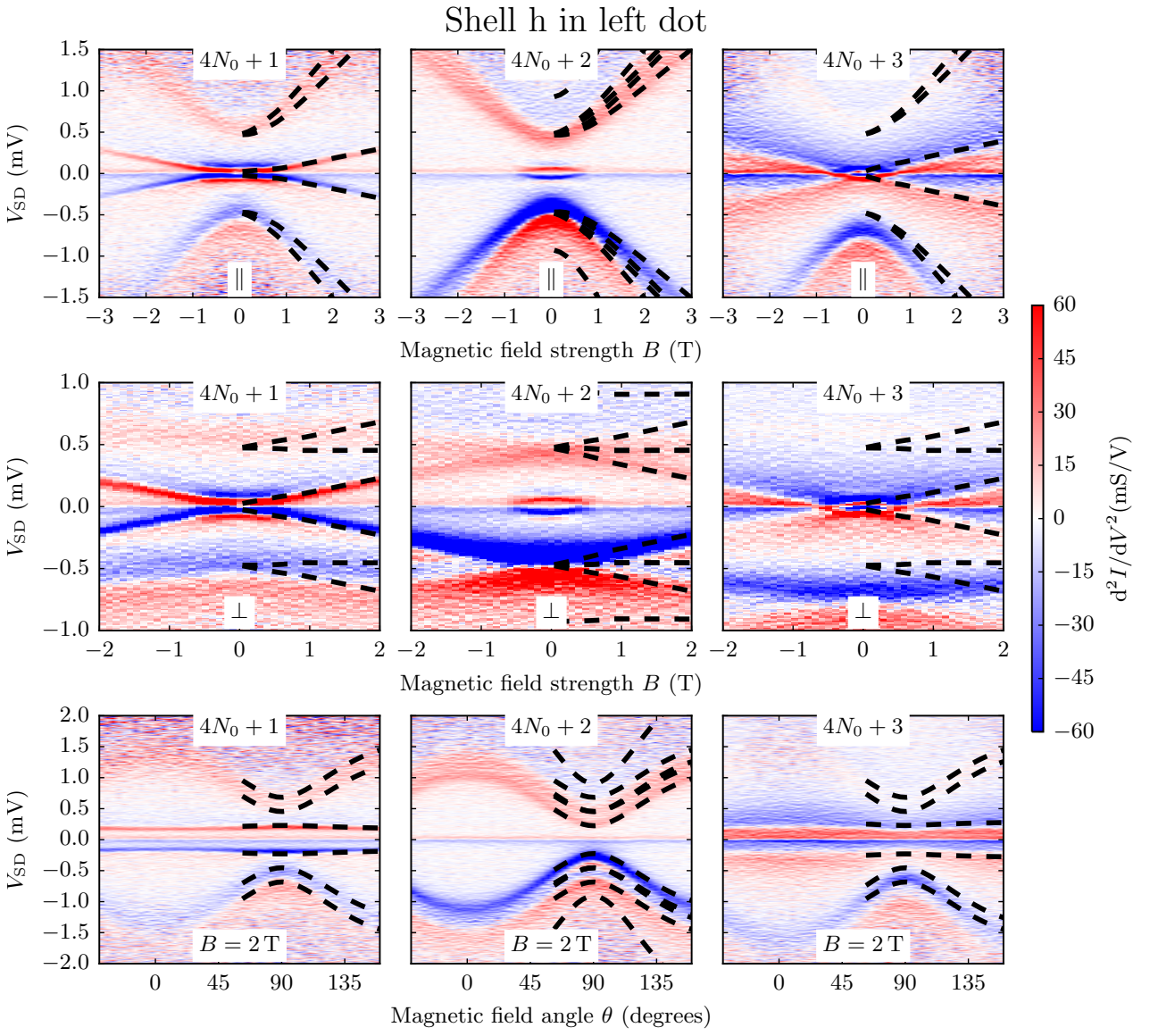

Figure 4.8: Excitation spectroscopy of shell h on the left side. The two top rows are parallel and perpendicular magnetic field sweeps. In the bottom row are sweeps of the magnetic field angle θ measured from the angle which is determined by fitting as being parallel for this particular shell. The correspondence between data and theory is good.

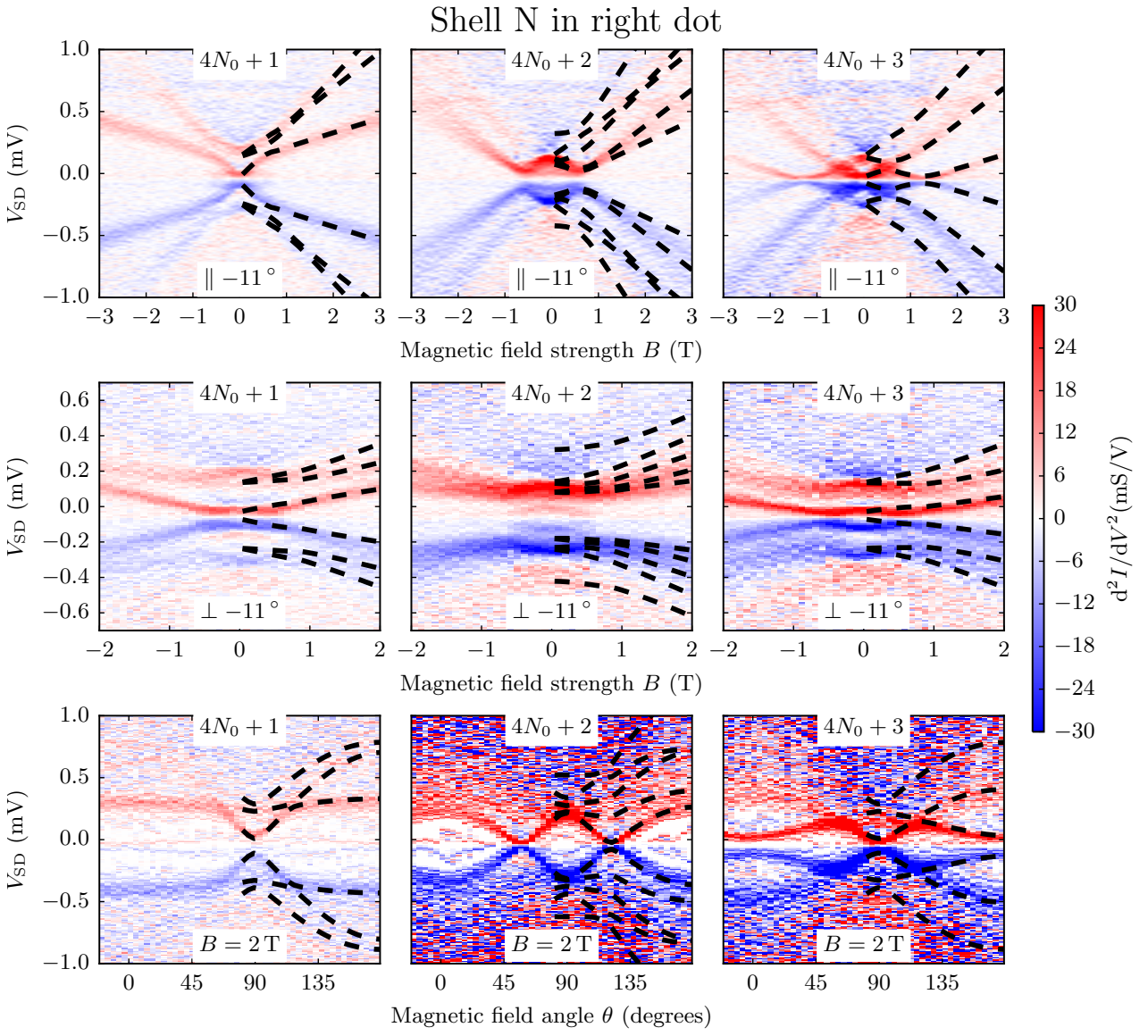

Figure 4.9: Excitation spectroscopy of shell N on the right side. The two top rows are parallel and perpendicular magnetic field sweeps offset by $-11°$ as indicated on the plots. In the bottom row are sweeps of the magnetic field angle θ measured from the angle which is determined by fitting as being parallel for this particular shell. The correspondence between data and theory is good.

Side	Shell	Δ_{SO} (µeV)	$\Delta_{KK'}$ (µeV)	gorb	J (µeV)	B_θ (degrees)	V_{BG} (V) for N=2
Right	b	140	220	1.4	0	15	-0.9
Right	c	-120	430	1.6	0	-5	-1.2
Right	d	160	50	1.3	0	5	-1.5
Right	M	140	220	2.1	0	-5	4.2
Right	N	150	70	2.6	120	3	4.5
Right	O	180	70	4.6	0	-13	4.8
Left	d	-70	530	5.2	0	18	-9.2
Left	g	-90	425	2.6	0	15	-10.1
Left	h	-50	370	5.2	0	22	-10.5
Left	i	-140	570	2.5	0	30	-10.8

Table 4.1: Table of parameters obtained from model fits. All fits also include the superconducting parameters $\Delta_{\mathrm{SC},0} = 60\,\mu\mathrm{eV}$ and $B_{\mathrm{C}} = 0.8\,\mathrm{T}$ through the function $\Delta_{\mathrm{SC}} = \Delta_{\mathrm{SC},0}\sqrt{1-(B/B_{\mathrm{C}})^2}$.

as follows: In a shell with occupation $N = 2$ the eigenstates are products of single-particle states[3]. Suppose the two-electron ground state in a non-degenerate shell is $|\tau s\rangle\,|\tau s'\rangle$. The highest energy state we can construct from single-particle states from the same shell is $|\tau' s'\rangle\,|\tau' s\rangle$. To go from one of these states to the other both electrons must change states. This makes the transition fourth, rather than second-order, in the intermediate state energy. Thus, the amplitude of this transition is reduced relative to cotunneling (second-order) processes and we don't observe the transition.

A common feature for all the magnetic field strength sweeps is the dip and peak around zero bias for $B < 0.8\,\mathrm{T}$. This reflects the suppression of current caused by the superconducting gap. The closing of this gap can be fitted to [22]

$$\Delta_{\mathrm{SC}}(B) = \Delta_{\mathrm{SC},0}\sqrt{1-(B/B_{\mathrm{C}})^2} \tag{4.4}$$

where the superconducting gap $\Delta_{\mathrm{SC},0} \approx 60\,\mu\mathrm{eV}$ and the critical in-plane field $B_{\mathrm{C}} \approx 0.6 - 0.8\,\mathrm{T}$ with reasonable correspondence. The fit is shown in Appendix B.3. The critical field is some 70 times higher than the bulk value of 10 mT [17] which is explained by the fact that the aluminium film is only 15 nm tall. We do not observe a superconducting feature in the angle sweeps since the constant magnetic field strength is higher than the critical field.

Using (2.14) we convert g_{orb}-values to diameters in the range 0.37-1.5 nm which is reasonable for the diameters expected for a nanotube[4]. A large variation is observed with adjacent shells in the left side differing by a factor of 2. In comparison with values found in the literature (cite cnt review) this is a small diameter, though. A correction to the estimate for the diameter can be made: The Fermi velocity is constant for the states we are considering and since we're filling states with increasing $k_\parallel$ the $k_\perp$ component must decrease correspondingly. Thus, $k_\perp$ and g_{orb} should be largest at the band gap where $k_\parallel$ is smallest. If we assume that

[3] Strictly, if the electron-electron interaction parameter $J \neq 0$ the eigenstates are not simple products. In our data J is so small that the argument is still approximately true.

[4] See, e.g., the carbon nanotube periodic table `https://www.quantumwise.com/documents/CNT_PeriodicTable.pdf`

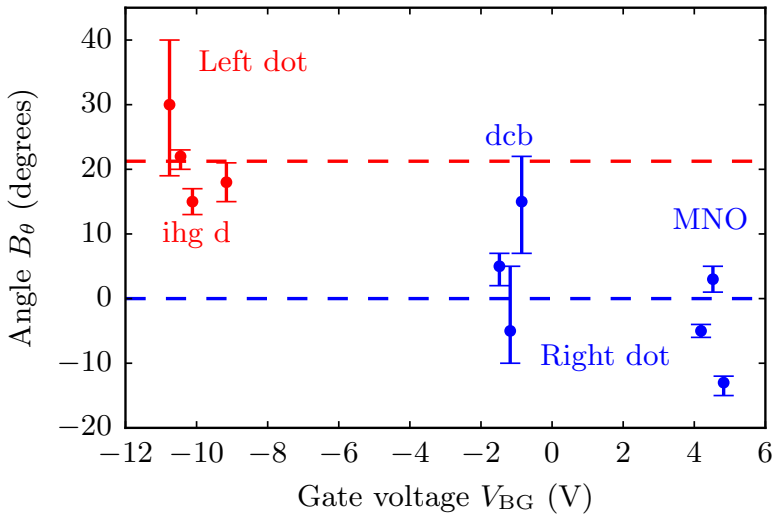

Figure 4.10: Fitted angles of the two sides as a function of backgate voltage. The error bars represent the range within which manual fitting of the parameters yielded a reasonable correspondence to data. Thus, they are somewhat subjective quantities. The large error bars on shells b and c are caused by low g_{orb}-values and hence small slopes in excitation spectroscopy data. Shell d has a very low value for $\Delta_{KK'}$ which ensures low uncertainty in fitting despite having a low g_{orb}-value. Some data is missing in shell i which increases its uncertainty.

The dashed lines indicate the average of the angles in the corresponding nanotube segment.

the band gap is around $V_{\mathrm{BG}} = 0$ but is simply too small to be readily observed we should see larger g_{orb}-values for the b, c, d shells than the other shells. This is in contrast to our observation and so the correction does not help explain the small diameter.

4.6 Angle comparison

The fitted angles for all shells are tabulated in Table 4.1. Initially, all angles are measured relative to the magnet axes in the cryostat. After parameter fitting the average of the angles of the right side is subtracted from all angles. We see from the table that the angles in the left side are larger than the right side by 21° on average.

Uncertainties on the angles are shown in Figure 4.10.

The angle difference is visualized in Figure 4.11. The angle of the blue line is the average of the angles in the right side. The red line is drawn as the tangent of the middle of the red side and thus illustrates the expected angle if the wave function in the left side is centered in the dot. Since the average angle of the left side shells of 21° is somewhat smaller than the 32° in the image we would expect the wave function in the left side shells to be closer to the superconductor. Supporting this expectation is the fact that the coupling to the superconductor in shells g, h and i is much stronger than to the normal lead as explained above. Shell d does not show this correspondence, although it also has an angle below 32°. From their angles we would expect shell O to be strongly coupled to the normal lead and shell b (right side) to be strongly coupled to the superconductor. This is in agreement with the bias spectroscopy

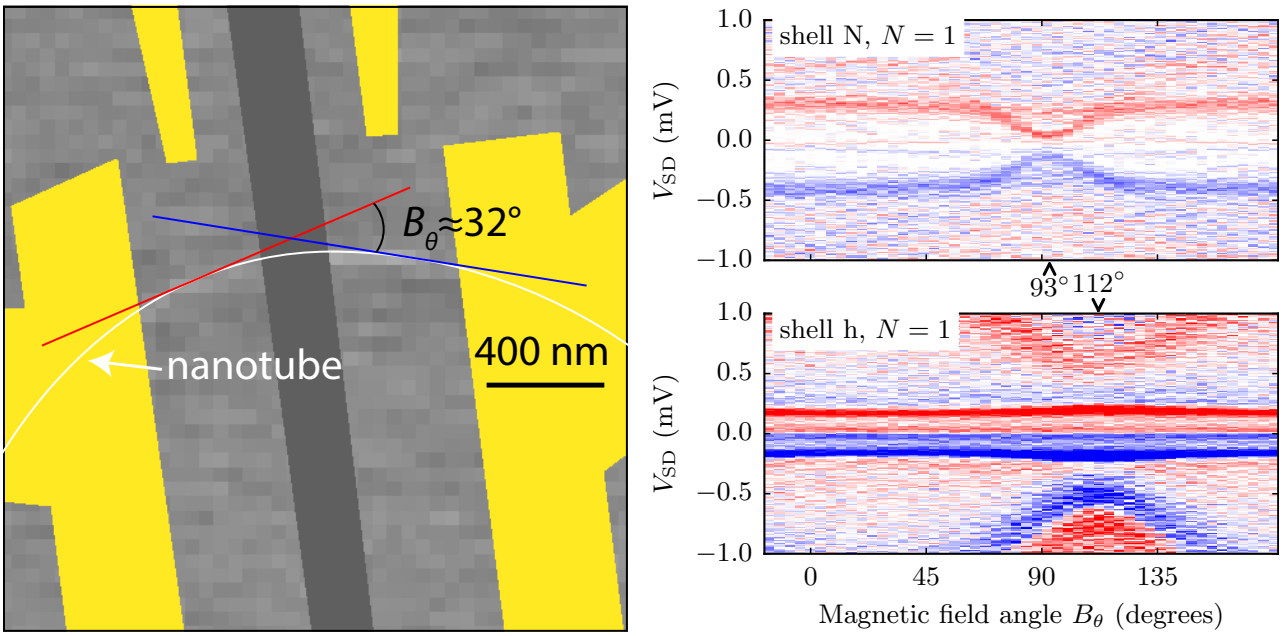

Figure 4.11: Left: SEM image showing the angle between the nanotube segments. The line on the right segment is defined by the average angle on the right side. The line in the left segment is drawn as the tangent at the middle of the left segment. Thus, $B_\theta \approx 32°$ represents the angle one would expect given the location of the dot in the right segment.

Right: Comparison of excitation spectroscopy of shells h and N for filling $N = 1$. The magnetic field is oriented perpendicular to the nanotube at the point where the first excitation in shell N and the second excitation in shell h are lowest in energy. This is shown to happen at 93° for shell N and 112° for shell h which are representative values for the average angle in the left and right segments.

in Figure 4.2 in which the diagonal pattern of these shells show that they are asymmetrically coupled like we expect. However, from the bias spectroscopy we would also expect shell d to have a large B_θ which is not the case. Measuring shells o, n, m, l which have the opposite coupling asymmetry from g, h and i would give further insight into a possible correlation between coupling and angle.

An example of the angle difference can be seen in Figure 4.11 which shows the excitation spectra of shells h and N at $N = 1$ side by side. The first excitation in shell N and the second excitation in shell h are at lowest energy at the angle at which the magnetic field is oriented perpendicular to the tube axis because it couples minimally with μ_{orb} at this angle. We see that this minimum splitting occurs at 93° for shell N and at 112° for shell h with a difference of 19° which is representative of the average angle difference.

Chapter 5

Conclusion and Outlook

In conclusion, a carbon nanotube Cooper pair splitter device was fabricated successfully. Measurements on the device at low temperature showed that it satisfies almost all the requirements for conducting an entanglement detection test, namely:

1. The device has clearly identifiable states owing to its four-fold symmetric appearance in a bias spectroscopy plot. In some places Kondo resonances mix the spin states which prevents or complicates entanglement detection.

2. A superconducting gap is present in the device.

3. The critical in-plane field of the superconductor is measured to 0.6-0.8 T which is approximately the same value as the spin-orbit magnetic field.

4. In the right nanotube segment the electronic spectrum is dominated by spin-orbit interaction in some shells. In the left dot spin-orbit interaction is observable in the spectrum, but it is dominated by disorder effects.

5. An average angle of 21° is determined between the spin-orbit magnetic fields of the left and right nanotube segment.

6. Non-local conductance measurements have been conducted, but they are inconclusive.

Due to fabrication challenges specific to carbon nanotubes, the most difficult requirement to satisfy (apart from the non-local measurements themselves) is obtaining a bent carbon nanotube which is dominated by spin-order in both its segments. The device presented in this thesis almost meets this requirement and preliminary measurements on subsequent devices indicate that similar high-quality devices may be obtained in reasonable yield.

Cooper pair splitting in a "basic" device without local magnetic fields or bends is still difficult. It is not well understood how parameters such as lead couplings, the superconducting gap or the charging energy influence the probability of Cooper pair splitting. Even with the requirements above satisfied the presence of a non-local signal depends on parameters that are not understood and in the case of a CNT-CPS also not controlled. Thus, although the advances presented in this thesis are promising entanglement detection following the Braunecker proposal remains a significant challenge.

Appendix A

Fabrication

A.1 Overview of fabrication

Four generations of samples were fabricated prior to gen5. A generation constitutes a single chip fabricated using a specific recipe. It contains a maximum of 48 potential CPS devices, fewer if bonding pads are used for 4-terminal measurements. Between generations the recipe was updated with whatever insights the previous generation offered.

The outline of the recipe (excluding the gen1 recipe) is as follows:

1. Make alignment marks.
2. Apply nanotube catalyst.
3. Grow nanotubes.
4. Use SEM to take images of nanotubes and design devices based on those images.
5. Make metal contacts.

A brief description of the generations is given below.

gen1 2-terminal devices were fabricated on one part of gen1 and characterized at low temperature. These devices were fabricated using the "blind" method where metal leads are put down to randomly contact nanotubes. Thus, no complex device geometries were possible on this part of gen1.

Another part of gen1 was used for fabricating CPS devices but those devices all turned out underexposed. A dose test determined the proper dose for subsequent generations.

gen2 Catalyst application problems ruined this chip during fabrication. A new method for catalyst application had to be developed be-

cause smaller catalyst islands than those used in gen1 are practical for CPS devices.

gen3 The nanotube concentration was very high on this chip so it was only used for testing lift-off of NbTiN. 2-terminal devices were fabricated with successful lift-off but they were not measured due to the high nanotube concentration.

gen4 CPS devices were completed without fabrication issues but no devices showed electric contact to the nanotubes. The width of the contacts and/or the type of the contacting metal were hypothesized to be the problem.

gen5 Devices were completed without fabrication issues and low temperature measurements were conducted successfully. The contacts were made wider ($\sim 100\,\text{nm}$ to $\sim 350\,\text{nm}$) and the contacting metal changed (accidentally, from Ti/Au to pure Au) to address the issues in gen4. The fabrication recipe for gen5 is given in detail in the next section.

A.2 Fabrication recipe for devA

devA was known as `cnt_gen5_FI` during fabrication.

1. Cut out $1.1\,\text{cm} \times 2.0\,\text{cm}$ chip with a $500\,\text{nm}$ SiO_2 top layer.
2. Sonicate chip in acetone. Flush with IPA and dry with nitrogen.
3. Bake chip on hot plate at $185\,^\circ\text{C}$ for 4 minutes.
4. Spin resists EL-6 and A4 at $4500\,\text{rpm}$ for 1 minute. Bake chip at $185\,^\circ\text{C}$ for 4 minutes between spinning EL-6 and A4 and after spinning A4.
5. Expose alignment mark pattern in the resist using an Elionix ELS-7000[1] and settings: Field size: $300\,\mu\text{m}$, dots: 20000, dose time: $0.22\,\mu\text{s}$, dose: $922\,\mu\text{C/cm}^2$, current: $10\,\text{nA}$, aperture $120\,\mu\text{m}$.
6. Develop chip in MIBK:IPA 1:3 for 90 seconds at room temperature, then 55 seconds in IPA at room temperature.
7. Ash 30 seconds before evaporating Ti/Pt (5/60 nm) in AJA evaporation chamber.
8. Lift-off in NMP at $80\,^\circ\text{C}$ in water bath for 25 minutes. Sonicate in NMP for 2 minutes and flush with transfer pipette.
9. Apply carbon nanotube catalyst to chip. See section below for details.
10. Grow CNTs at $910\,^\circ\text{C}$ for 18 minutes. See section below for details.

[1] The ELS-7000 operates at an acceleration voltage of 100 kV while the minimum energy required to knock out a carbon atom of the nanotube is estimated at 86 keV [23]. Thus, the Raith eLine (variable acceleration voltage, but typically 20 kV) was used exclusively after nanotube growth to avoid damaging the nanotubes.

11. Take images of carbon nanotubes in SEM at an acceleration voltage of 1.5 kV. Use the following image properties: Size: 100 µm × 100 µm, resolution: 2000 points × 2000 points, point average: 1.

12. Design devices based on SEM images. DesignCad 23 was used for this purpose.

13. Flush chip in acetone and then IPA. Dry with nitrogen. Sonication should be avoided when CNTs are on the chip.

14. Spin resist EL-6 and A4 as in point 4.

15. Expose pattern for normal contacts in the resist using Raith eLine. **Settings for inner contacts**: Area step: 4 nm, dose: 390 µC/cm^2, Write field size: 100 µm, Aperture: 30 µm, Acceleration voltage: 20 kV. **Settings for outer contacts**: Area step: 20 nm, dose: 390 µC/cm^2, Write field size: 200 µm, Aperture: 120 µm, Acceleration voltage: 20 kV.

16. Develop chip in MIBK:IPA 1:3 for 55 seconds at room temperature, then 55 seconds in IPA at room temperature.

17. Evaporate Au on the chip using Edwards Auto 306 thermal evaporator.

18. Spin resist EL-6 and A4 as in point 4.

19. Expose pattern for superconducting contacts in the resist using Raith eLine. **Settings for inner contacts**: Area step: 4 nm, dose: 390 µC/cm^2, Write field size: 100 µm, Aperture: 30 µm, Acceleration voltage: 20 kV. **Settings for outer contacts**: Area step: 20 nm, dose: 390 µC/cm^2, Write field size: 200 µm, Aperture: 120 µm, Acceleration voltage: 20 kV.

20. Develop chip in MIBK:IPA 1:3 for 55 seconds at room temperature, then 55 seconds in IPA at room temperature.

21. Evaporate Ti/Al on the chip in AJA evaporation chamber.

If the metals used for the device are not suitable for bonding an additional lithography step is required to define bonding pads. This was the case for the fabrication of devA where an additional lithography step of Ti/Au 10/90 nm was done. Generally, the Au lithography step (point 15) should be last because Au doesn't adhere well to the chip surface.[2] The reason that it's not the last step in the recipe above is that the intention was to deposit titanium as a sticking layer below the gold. This did not work out for various reasons.

[2] This is even more of a problem when using leads made of Pd which adheres very poorly to the chip surface.

A.3 Deposition of carbon nanotube catalyst

It took a few tries to figure out an efficient way of depositing the CNT catalyst on the wafer. The below recipe was found to work consistently for the catalyst consisting of iron nitrate ($Fe(NO_3)_3$) molybdenum acetate and alumina support particles[3]. Note that this recipe is designed for dot exposures in a Raith eLine. It consistently yielded catalyst dots with radii of 2 µm with little to no catalyst contamination on the rest of the chip. It might not work with area exposures below a certain size unless the exposure parameters are changed.

[3] The catalyst itself was presented in Kong *et al.* [24].

1. Spin A6 PMMA at 4500rpm for 1 minute.
2. Bake at 185 °C for 1 minute.
3. Spin another layer of A6 PMMA at 4500rpm for 1 minute to yield a double-layer of A6.
4. Bake at 185 °C for 1 minute.
5. Expose catalyst pattern using dot exposure with parameters: Dose: 350 µC/cm^2, area step: 10 nm, dot dose: 0.1 pA, write field: 200 µm, acceleration voltage: 20 kV, aperture: 30 µm. It is important in this step that you scan as little as possible on the chip when finding alignment marks and aligning. If possible you should know the distance from an alignment mark to the corner of your chip and jump directly to it rather than searching for it. Accidentally exposing resist promotes sticking of catalyst to the chip in that spot. Catalyst that sticks accidentally to the chip is typically more prone to being scattered on the chip in subsequent steps.
6. Develop for 55 seconds in MIBK:IPA 1:3, then 55 seconds in IPA.
7. Stir catalyst solution for 2 minutes or more.
8. For a 1 cm × 2 cm chip apply 4 drops of catalyst using a transfer pipette.
9. Let the chip dry under a petri dish for about 11 minutes. The duration is probably not important as long as the chip is completely dry. The purpose of the petri dish is to avoid stray drops of liquid hitting the chip.
10. Bake the chip for 7 minutes[4] at 185 °C.
11. Lift-off in 100 mL NMP for two hours at 76 °C.
12. At this point the chip can be sonicated if it is absolutely necessary. Sonication is efficient in removing catalyst resting on resist, but it

[4] This step was crucial.

also shakes loose and scatters catalyst resting on the chip. Typically, sonication is not necessary if the chip has been soaking in NMP long enough at 76 °C.

13. Spray the chip thoroughly with acetone to remove unwanted catalyst residues before moving the chip to IPA and drying it.

A.4 Growth of carbon nanotubes

Carbon nanotubes were grown in a Carbolite MTF 12/25/400 CVD oven. A "prebake" step is done with the oven empty before doing an actual growth. The purpose of the prebake step is to flush the oven of contaminants. The gas flow was configured as follows[5]:

[5] Conversion to the percentages used in the lab on the Brooks controller: gas flow = percentage × max flow. Max flows are: Ar: 2, H_2: 0.5, and CH_4: 5 nL/min N_2. For instance the Ar flow of 0.8 nL/min N_2 corresponds to 40%.

			Gas flow (nL/min N_2)		
Time (minutes)	T_{set} (°C)	T_{oven} (°C)	Ar	H_2	CH_4
0	900	23	0.8	–	–
65	0	900	0.8	–	–

After the second step in the table above the oven is cooled to a couple of hundred degrees Celsius before loading the chip and doing the growth:

			Gas flow (nL/min N_2)		
Time (minutes)	T_{set} (°C)	T_{oven} (°C)	Ar	H_2	CH_4
0	900	376	2	–	–
5	900	665	0.8	0.1	–
20	900	900	–	0.1	–
30	900	900	–	0.1	0.65
49	0	900	0.8	–	–

The concentration of nanotubes after the first growth was considered to be too low for designing devices. Therefore, the chip was ashed for 1 minute to remove the nanotubes and a second growth was done:

			Gas flow (nL/min N_2)		
Time (minutes)	T_{set} (°C)	T_{oven} (°C)	Ar	H_2	CH_4
0	910	246	2	–	–
5	910	?	0.8	–	–
21	910	910	–	0.1	–
31	910	910	–	0.1	0.65
49	0	910	0.8	–	–

In the second growth the H_2 gas was inadvertently not turned on in the second step. Also, the temperature was increased from 900 °C to 910 °C to increase the concentration of nanotubes. This decision was based on a gut feeling, though, since no obvious correlation between temperature and nanotube concentration was found in this project. The

variability in nanotube concentration was found to be very large, from about 1 to $\sim$ 100 per 100 µm $\times$ 100 µm for the same type of growth. Quite often, the second growth in a sequence like the one above yielded good nanotube concentrations. Ashing between the first and second growths may play a role for this effect.

A.5 Material considerations for CNT devices

Since carbon nanotubes are grown at high temperatures the choice of materials for devices is not unlimited. In this project the structures that had to withstand CNT growth were mostly alignment marks but preferably also bonding pads and part of the device leads because it simplifies fabrication. To speed up the fabrication process we preferred to use a the same material combination for all structures. When subjected to CNT growth the material combination should

1. maintain its shape (important for alignment marks and leads),
2. not cause back gate leaks (important for bonding pads and leads),
3. allow for bonding (important for bonding pads).

Our starting point of Ti/Pt on SiO2 (which is used on devA) wasn't able to maintain its shape and it also caused back gate leaks. Given both metals' rather high melting points of about 1700 °C this was surprising. This characteristic agglomeration of Ti/Pt has also been found elsewhere, though[25].

After trying various combinations of metals and substrates we decided to use a stack of SiO_2/W/Pt which has previously been found to work well [26]. Even this metal stack does not work consistently enough that we could use it for bonding pads and leads. At the time of writing we're only using it for alignment marks for which it serves it purpose well.

Appendix B

Supplemental data

B.1 Supplemental data

Data used for fitting parameters in some table.

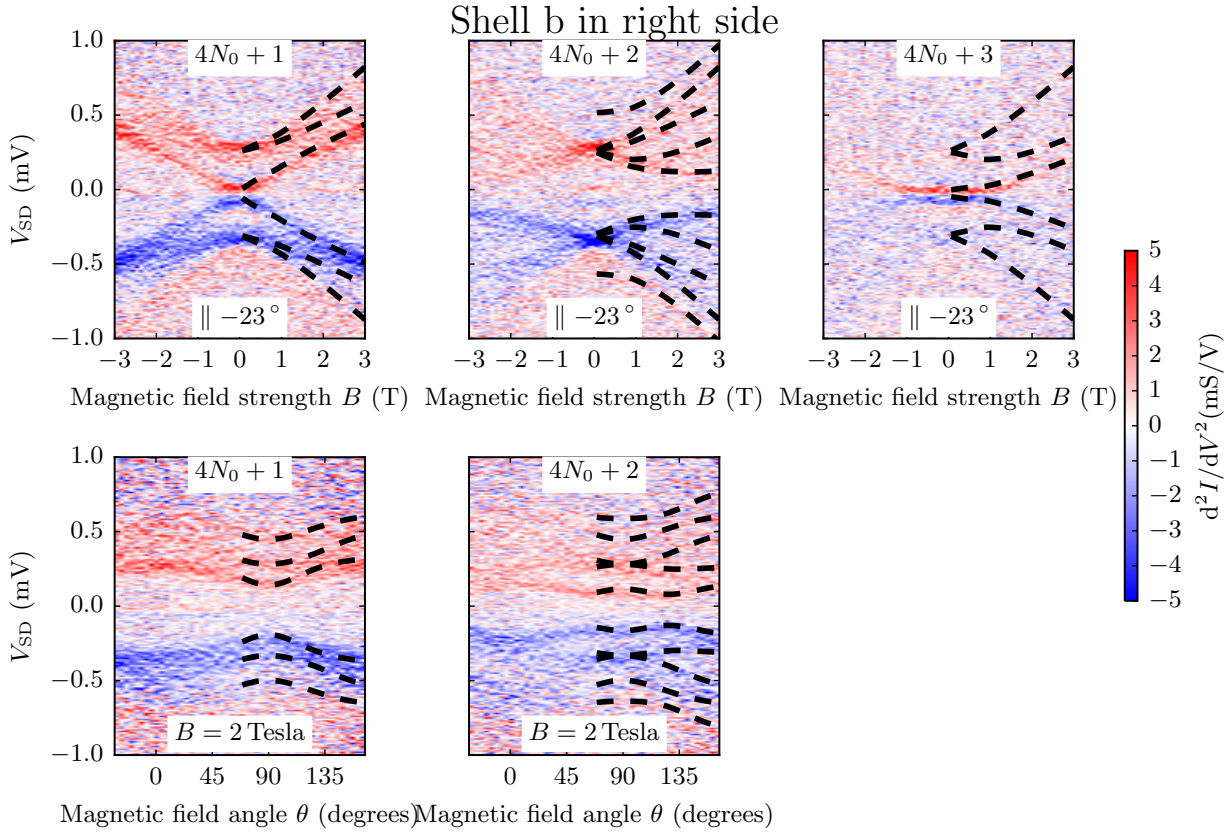

Figure B.1: Excitation spectroscopy of shell b on the right side. Not all combinations of filling and magnetic field were measured. The top rows are parallel magnetic field sweeps offset by $-23°$ as indicated on the plots. In the bottom row are sweeps of the magnetic field angle θ measured from the angle which is determined by fitting as being parallel for this particular shell.

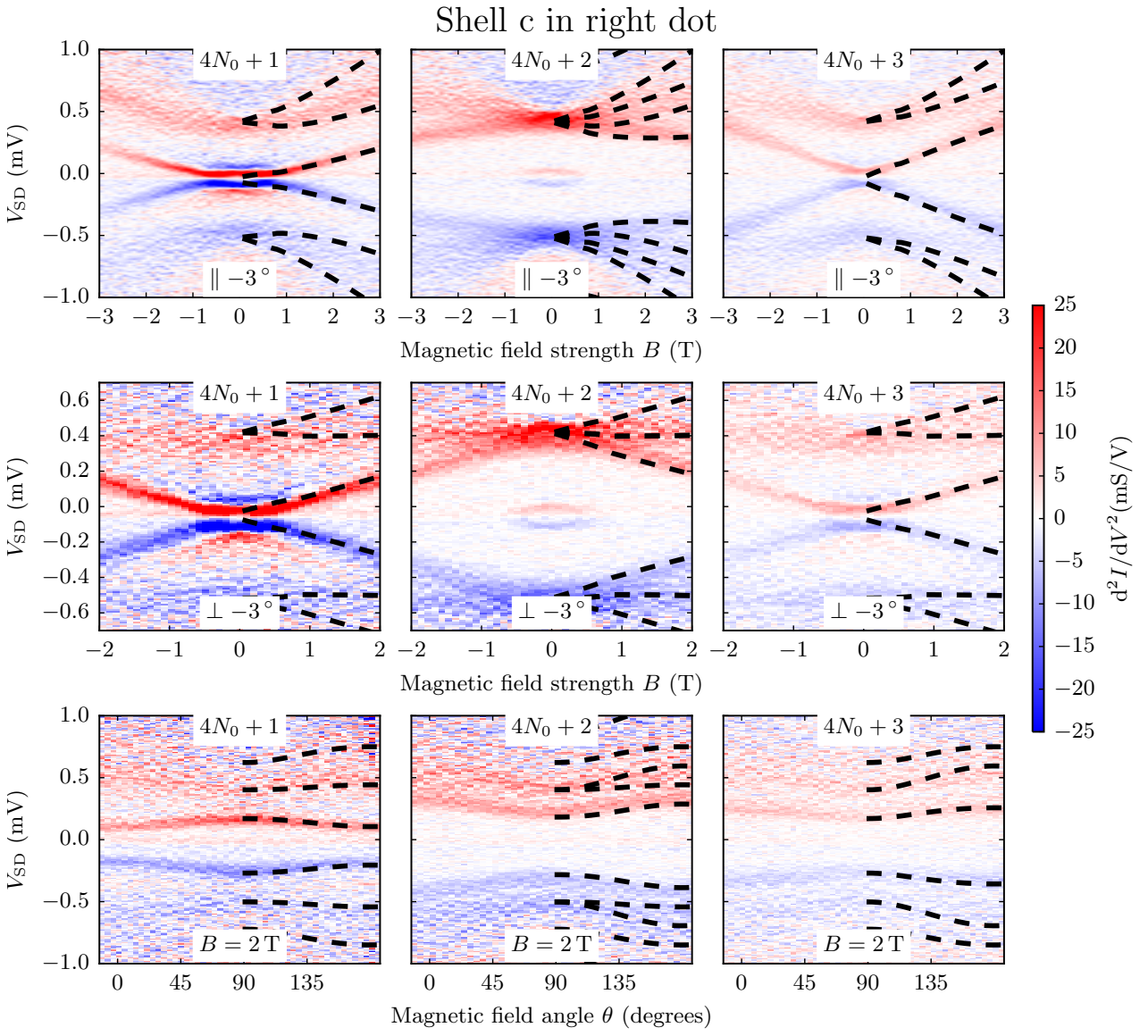

Figure B.2: Excitation spectroscopy of shell c on the right side. The two top rows are parallel and perpendicular magnetic field sweeps offset by $-3°$ as indicated on the plots. In the bottom row are sweeps of the magnetic field angle θ measured from the angle which is determined by fitting as being parallel for this particular shell.

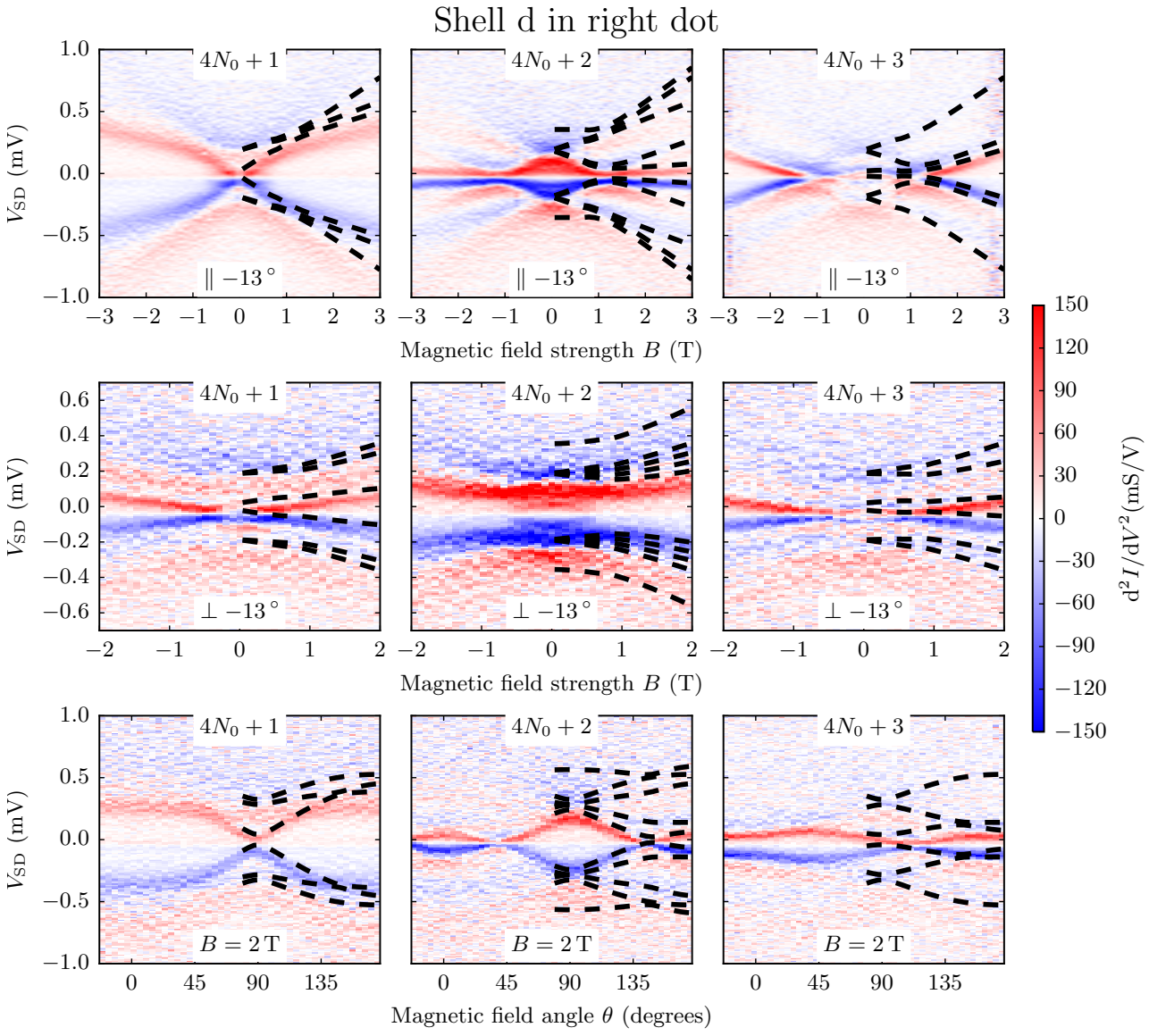

Figure B.3: Excitation spectroscopy of shell d on the right side. The two top rows are parallel and perpendicular magnetic field sweeps offset by $-13°$ as indicated on the plots. In the bottom row are sweeps of the magnetic field angle θ measured from the angle which is determined by fitting as being parallel for this particular shell.

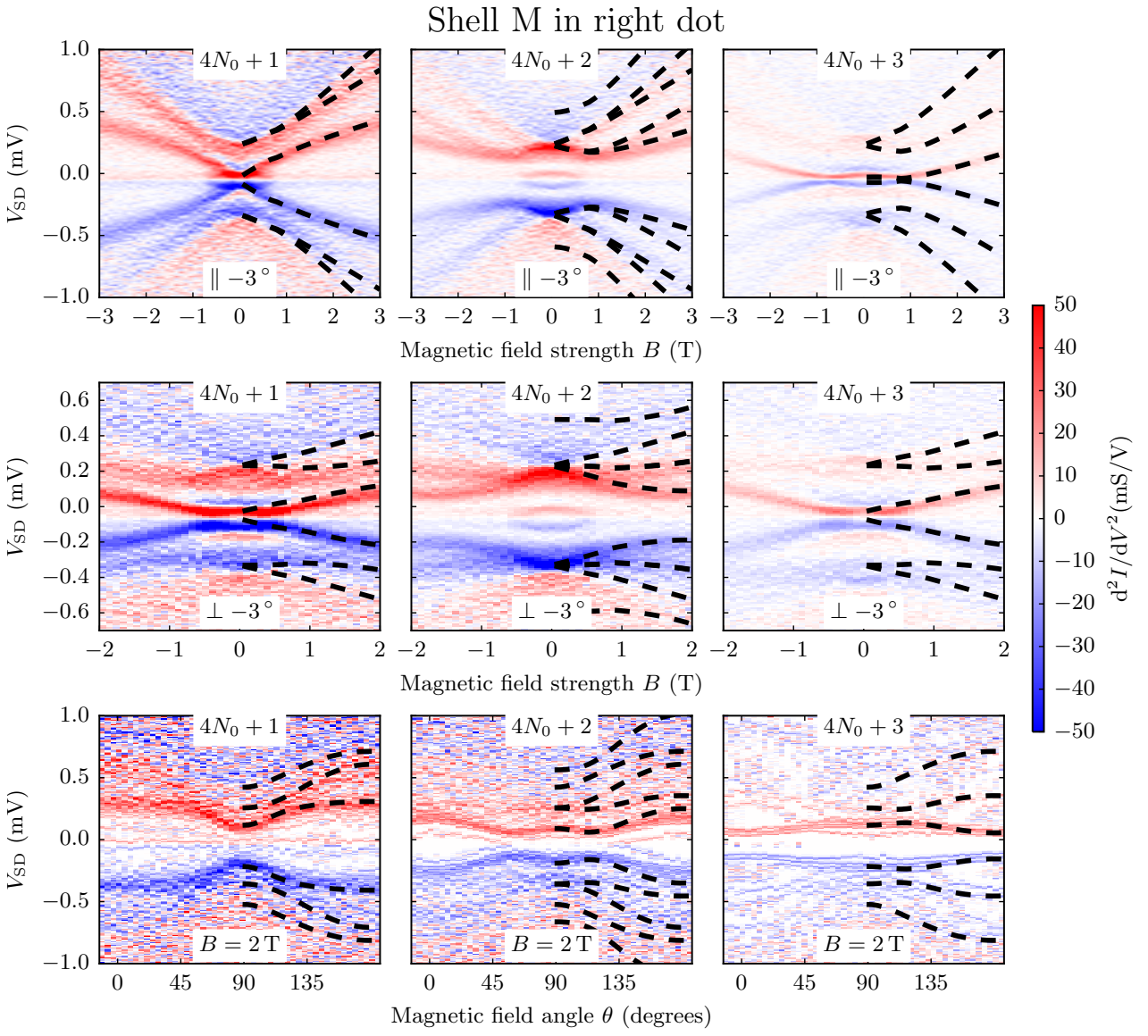

Figure B.4: Excitation spectroscopy of shell M on the right side. The two top rows are parallel and perpendicular magnetic field sweeps offset by $-3°$ as indicated on the plots. In the bottom row are sweeps of the magnetic field angle θ measured from the angle which is determined by fitting as being parallel for this particular shell.

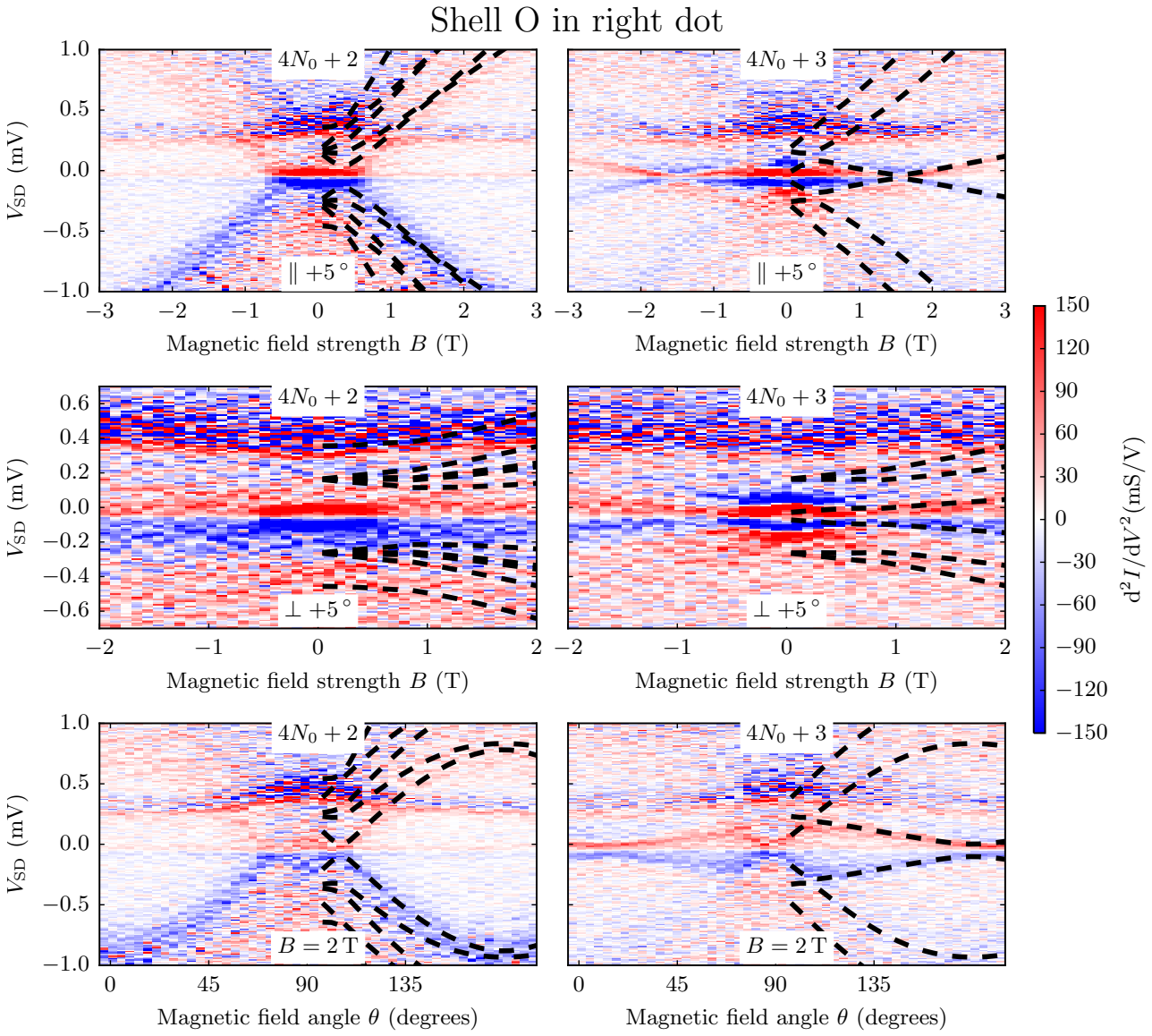

Figure B.5: Excitation spectroscopy of shell O on the right side. Data for $N = 1$ is not available. The two top rows are parallel and perpendicular magnetic field sweeps offset by 5° as indicated on the plots. In the bottom row are sweeps of the magnetic field angle θ measured from the angle which is determined by fitting as being parallel for this particular shell.

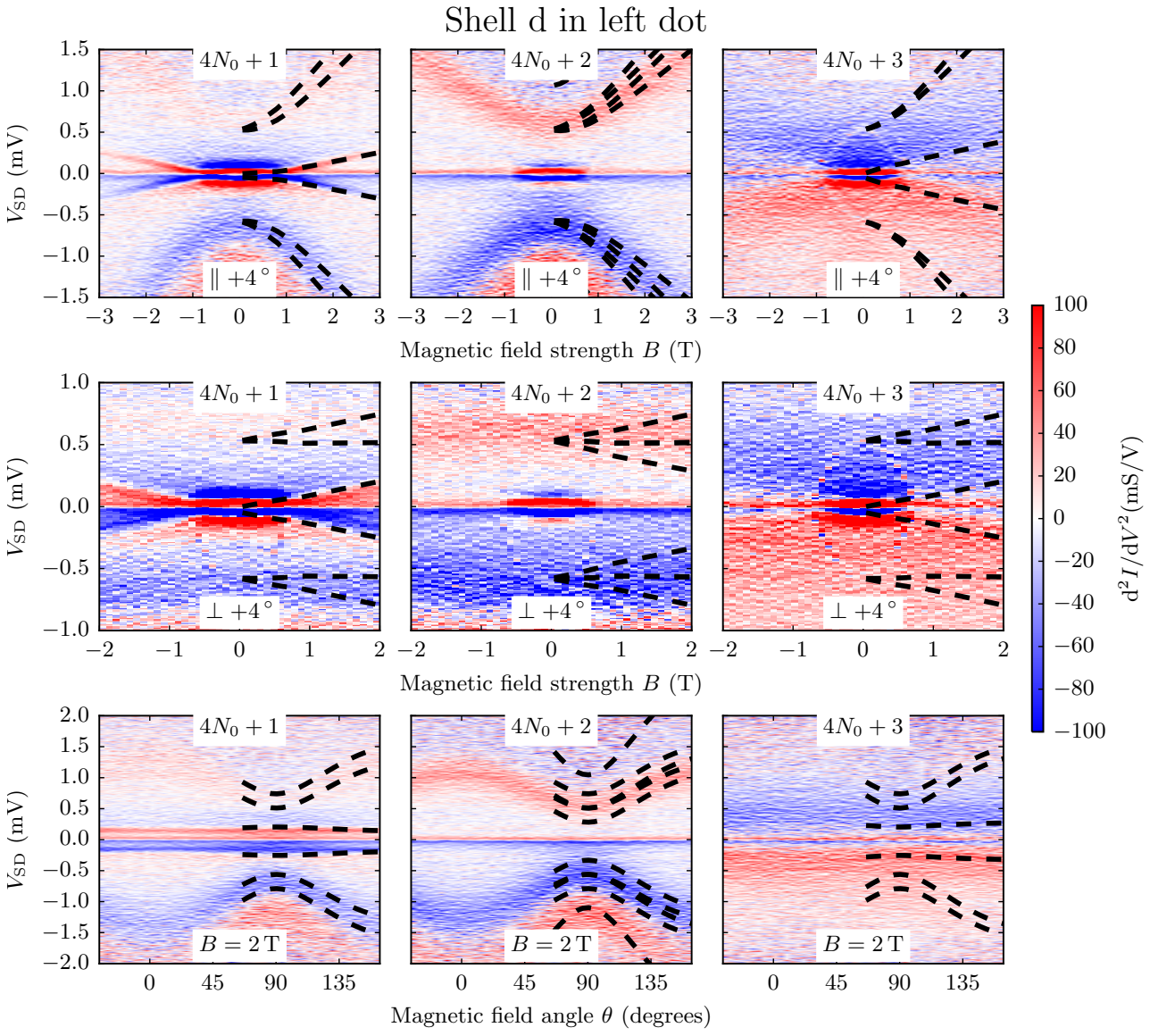

Figure B.6: Excitation spectroscopy of shell d on the left side. The data which supposedly represents $N = 3$ is taken at the wrong gate voltage, probably due to a switch. The two top rows are parallel and perpendicular magnetic field sweeps offset by 4° as indicated on the plots. In the bottom row are sweeps of the magnetic field angle θ measured from the angle which is determined by fitting as being parallel for this particular shell.

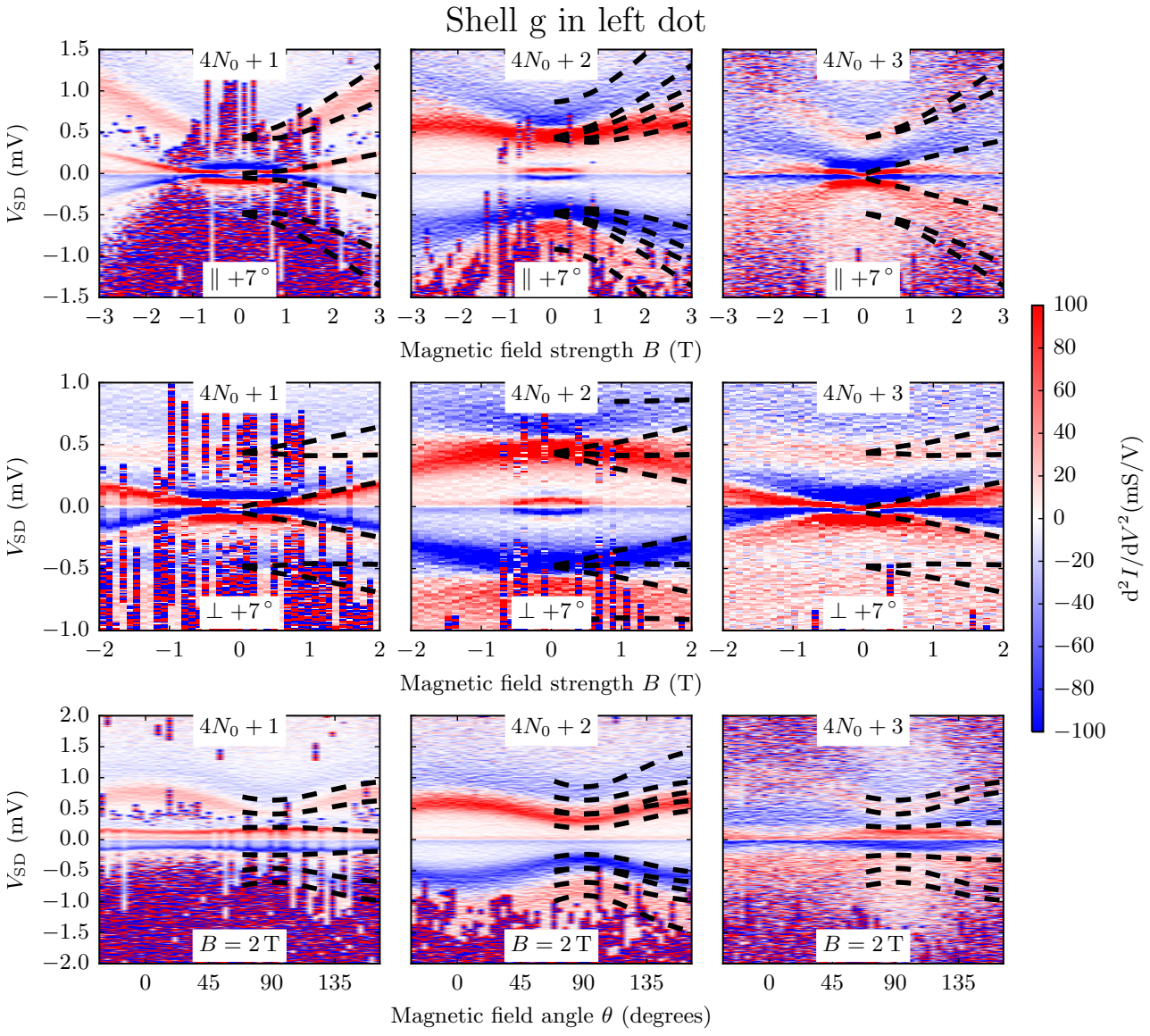

Figure B.7: Excitation spectroscopy of shell g on the left side. The two top rows are parallel and perpendicular magnetic field sweeps offset by 7° as indicated on the plots. In the bottom row are sweeps of the magnetic field angle θ measured from the angle which is determined by fitting as being parallel for this particular shell. The cause of the high noise level is unknown.

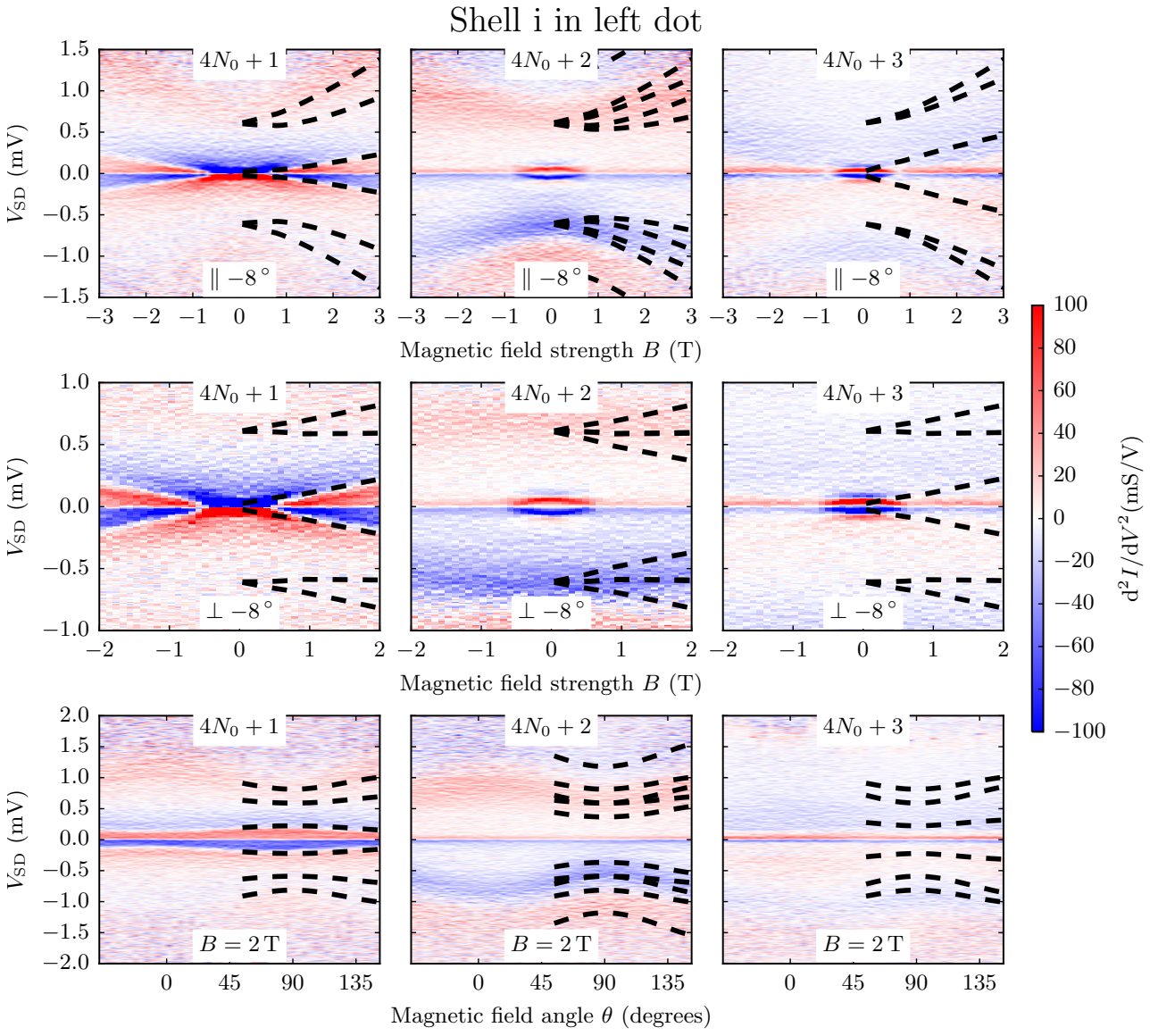

Figure B.8: Excitation spectroscopy of shell i on the left side. The data which supposedly represents $N = 3$ is either taken at the wrong gate voltage or inelastic cotunneling is suppressed at this particular filling. The two top rows are parallel and perpendicular magnetic field sweeps offset by $-8°$ as indicated on the plots. In the bottom row are sweeps of the magnetic field angle θ measured from the angle which is determined by fitting as being parallel for this particular shell.

B.2 Uncertainties for fitted parameters

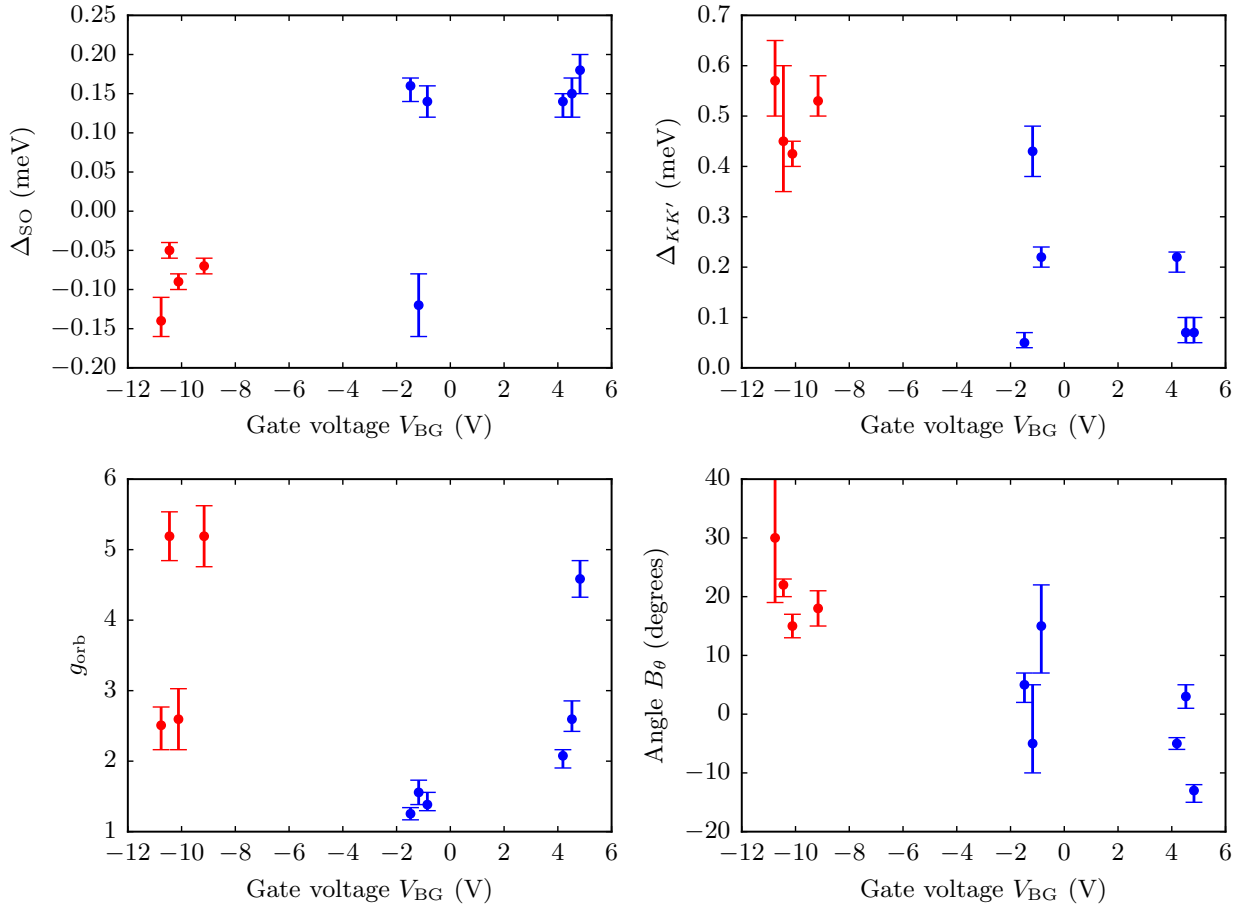

Figure B.9: Overview of fitted parameters with uncertainties. The error bars represent the range within which manual fitting of the parameters yielded a reasonable correspondence to data. Thus, they are somewhat subjective quantities.

B.3 Closing of superconducting gap with magnetic field

Magnetic field in the z-direction The z-direction is approximately parallel to horizontal in Figures 3.1 and 4.11.

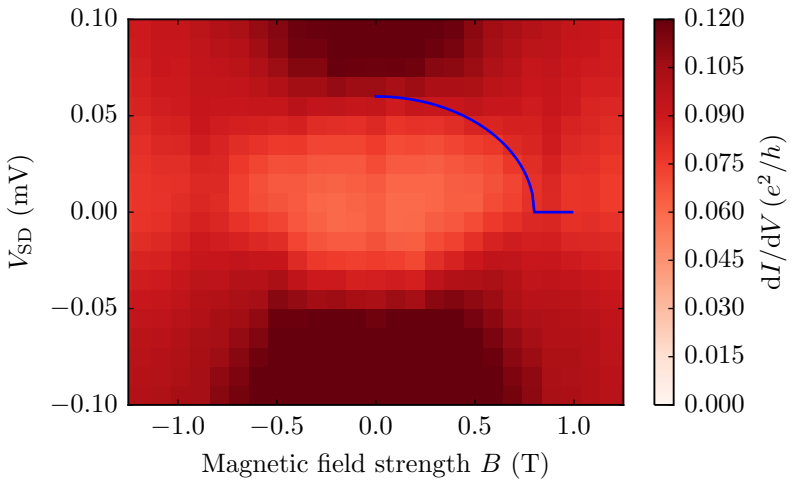

Figure B.10: Closing of superconducting gap with magnetic field in the z-direction. The line represents $\Delta_{SC}(B) = \Delta_{SC,0}\sqrt{1-(B/B_C)^2}$ with $\Delta_{SC,0} \approx 60\,\mu eV$ and $B_C \approx 0.8\,T$.

Magnetic field in the x-direction The x-direction is approximately perpendicular to horizontal in Figures 4.11 and 3.1.

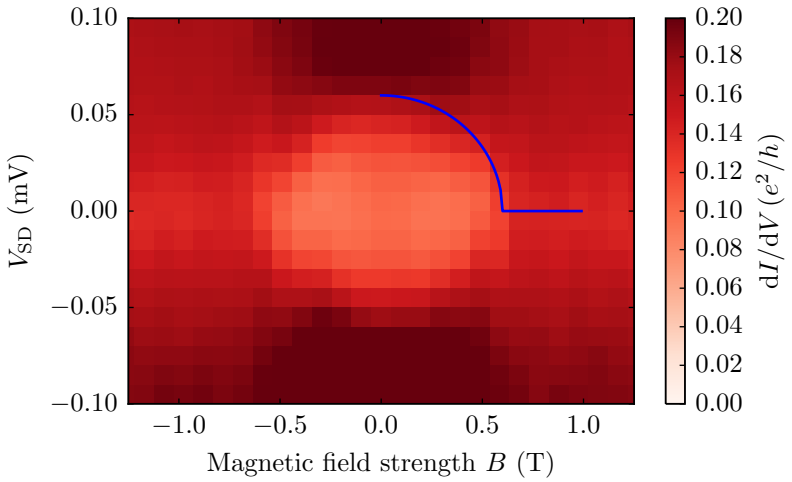

Figure B.11: Closing of superconducting gap with magnetic field in the x-direction. Closing of superconducting gap with magnetic field in the z-direction. The line represents $\Delta_{SC}(B) = \Delta_{SC,0}\sqrt{1-(B/B_C)^2}$ with $\Delta_{SC,0} \approx 60\,\mu eV$ and $B_C \approx 0.6\,T$.

Bibliography

1. Braunecker, B., Burset, P. & Levy Yeyati, A. Entanglement detection from conductance measurements in carbon nanotube cooper pair splitters. *Physical Review Letters* **111,** 136806. ISSN: 00319007 (Sept. 2013).
2. Herrmann, L. G. *et al.* Carbon Nanotubes as Cooper-Pair Beam Splitters. *Physical Review Letters* **104,** 026801. ISSN: 0031-9007 (Jan. 2010).
3. Schindele, J., Baumgartner, A. & Schönenberger, C. Near-Unity Cooper Pair Splitting Efficiency. *Physical Review Letters* **109,** 157002. ISSN: 0031-9007 (Oct. 2012).
4. Hofstetter, L., Csonka, S., Nygård, J. & Schönenberger, C. Cooper pair splitter realized in a two-quantum-dot Y-junction. *Nature* **461,** 960–3. ISSN: 1476-4687 (Oct. 2009).
5. Das, A. *et al.* High-efficiency Cooper pair splitting demonstrated by two-particle conductance resonance and positive noise cross-correlation. *Nature communications* **3,** 1165. ISSN: 2041-1723 (Jan. 2012).
6. Fülöp, G. *et al.* Local electrical tuning of the nonlocal signals in a Cooper pair splitter, 1–9 (2014).
7. Grove-rasmussen, K. Electronic Transport in Single Wall Carbon Nanotubes University of Copenhagen. *Thesis, Ph D* (2006).
8. Kuemmeth, F., Ilani, S., Ralph, D. C. & McEuen, P. L. Coupling of spin and orbital motion of electrons in carbon nanotubes. *Nature* **452,** 448–52. ISSN: 1476-4687 (Mar. 2008).
9. Churchill, H. O. H. *et al.* Relaxation and dephasing in a two-electron C13 nanotube double quantum dot. *Physical Review Letters* **102,** 2–5. ISSN: 00319007 (2009).
10. Lai, R. a., Churchill, H. O. H. & Marcus, C. M. g-Tensor Control in Bent Carbon Nanotube Quantum Dots. *Physical Review B* **89,** 121303. ISSN: 1098-0121 (2014).
11. Laird, E. a. *et al.* Quantum transport in carbon nanotubes. *Reviews of Modern Physics* **87,** 703–764. ISSN: 0034-6861 (2015).

12. Kanoun, O. *et al.* Flexible Carbon Nanotube Films for High Performance Strain Sensors. *Sensors* **14,** 10042–10071. ISSN: 1424-8220 (2014).

13. Reynoso, A. a. & Flensberg, K. Dephasing and hyperfine interaction in carbon nanotube double quantum dots: The clean limit. *Physical Review B* **84,** 1–20. ISSN: 1098-0121 (2011).

14. Bruus, H. & Flensberg, K. *Many-body Quantum Theory in Condensed Matter Physics* (Oxford University Press, 2004).

15. Ihn, T. *Semiconductor Nanostructures* (Oxford University Press, 2010).

16. Kondo, J. Resistance Minimum in Dilute Magnetic Alloys. *Progress of Theoretical Physics* **32,** 37–49. ISSN: 0033-068X (1964).

17. Kittel, C. *Introduction to Solid State Physics* 8th (John Wiley & Sons, Inc., 2005).

18. Jespersen, T. S. *et al.* Gate-dependent spin-orbit coupling in multielectron carbon nanotubes. *Nature Physics* **7,** 348–353. ISSN: 1745-2473 (2010).

19. Cleuziou, J. P., N'guyen, N. G., Florens, S. & Wernsdorfer, W. Interplay of the kondo effect and strong spin-orbit coupling in multihole ultraclean carbon nanotubes. *Physical Review Letters* **111,** 1–5. ISSN: 00319007 (2013).

20. Schmid, D. R. *et al.* Broken SU(4) symmetry in a Kondo-correlated carbon nanotube. *Physical Review B* **91,** 155435. ISSN: 1098-0121 (2015).

21. Steele, G. a. *et al.* Large spin-orbit coupling in carbon nanotubes. *Nature communications* **4,** 1573. ISSN: 2041-1723 (Jan. 2013).

22. Douglass, D. H. Magnetic Field Dependence of the Superconducting Energy Gap. *Physical Review Letters* **6,** 346–348 (1961).

23. Smith, B. W. & Luzzi, D. E. Electron irradiation effects in single wall carbon nanotubes. *Journal of Applied Physics* **90,** 3509–3515. ISSN: 00218979 (2001).

24. Kong, J., Soh, H. T., Cassel, a. M., Quate, C. F. & Dai, H. Synthesis of indicidual single-walled carbon nanotubes on patterned silicon wafers. *Nature* **395,** 878. ISSN: 0028-0836 (1998).

25. Schmid, U. The impact of thermal annealing and adhesion film thickness on the resistivity and the agglomeration behavior of titanium/platinum thin films. *Journal of Applied Physics* **103,** 054902. ISSN: 00218979 (2008).

26. Churchill, H. O. H. *Quantum Dots in Gated Nanowires and Nanotubes* PhD thesis (Harvard University, 2012).